Critical current measurements of TFMC-LMI and CSMC-VAC Nb_3Sn—measurements, FEA corrections and the scaling law parameterisation

DMJ Taylor, P Foley, HJ Niu and DP Hampshire

Superconductivity Group, Department of Physics, University of Durham, South Road, Durham DH1 3LE, UK

Extension to Contract. Nos.: EFDA/03-1103. September 2003–April 2004

1. *The scaling law for the strain-dependence of the critical current density in Nb_3Sn superconducting wires* D. M. J. Taylor and D. P. Hampshire, (In progress Sep. 2004).
2. *Properties of helical springs used to measure the effect of axial strain on the critical current density of superconducting wires* D. M. J. Taylor and D. P. Hampshire, Supercond. Sci. Tech. (submitted Sep. 2004).
3. *Effect of axial strain cycling on the critical current density and n-value of ITER niobium-tin wires* D. M. J. Taylor and D. P. Hampshire, Physica C **401**, 40 (2004).

Photograph of a superconducting wire mounted on a tee-shaped spring.

Acknowledgements

It is noted that much of the work presented in this report has been included as part of the doctoral thesis submitted by David Taylor at Durham University. The publications that have been produced in the course of producing work include: (i) *The scaling law for the strain-dependence of the critical current density in Nb_3Sn superconducting wires* D. M. J. Taylor and D. P. Hampshire, (submitted Sep. 2004). (ii) *Properties of helical springs used to measure the effect of axial strain on the critical current density of superconducting wires* D. M. J. Taylor and D. P. Hampshire, Supercond. Sci. Tech. (submitted Sep. 2004).

The authors acknowledge the help and support of N Mitchell, E Salpietro, A Portone and A Vostner and the very helpful discussions with Roberto Zanino.

We also acknowledge the many discussions we have had with those in the community including: D. Bessette, D. Bruzzone, N. Cheggour, J. Duchateau, J. Ekin, W H Fietz, H. Fillunger, B. Karlemo, P. Komarek, R. Maix, N Martovetsky, J. Minervini, A. Nyilas, A Nijhuis, A. Portone, K. Osamura, L. Savoldi Richard, J. Schultz and A. Ulbricht.

Extended abstract

The two primary tasks outlined in this report are:

i) A characterisation of the critical current density as a function of magnetic field, temperature and strain ($J_C(B,T,\varepsilon)$) of the VAC-CSMC strand.
ii) A characterisation of $J_C(B,T,\varepsilon)$ of the LMI-TFMC strand.

The numerical parameterisation required for magnet engineering purposes for both of these strands are presented in Appendix I of this report—also parameterisations of data for a Furukawa Nb_3Sn ITER strand, a Sumitomo Nb_3Al strand and an OST strand are included. These parameterisations include FEA corrections.

We have investigated the optimised design of helical springs for making $J_C(B,T,\varepsilon)$ measurements and used finite element analysis to analyse the spatial strain profile obtained throughout a twisted helical spring. It is demonstrated that the strain gradient across the wire is small when using tee-shaped springs and can be corrected for using finite element analysis. Supplementing previous work by Walters *et al.*, we recommend springs made with highly elastic materials (e.g. Ti-6Al-4V), optimised tee-shaped cross-sections, and optimum integer numbers of turns (e.g. 4 or 5) to give the best performance in relation to the transverse and longitudinal strain uniformity in the wire.

Comprehensive $J_C(B,T,\varepsilon)$ data are presented for the EM-LMI and Vac Nb_3Sn superconducting wires used in the two ITER model coils. Various consistency tests demonstrate good interlaboratory agreement and that J_C is a single-valued function of B, T, and ε. For high-upper-critical-field (28–30 T) Nb_3Sn wires such as those intended for ITER, we report an approximately universal relationship between normalised $B^*_{C2}(0)$ and intrinsic strain, and a power-law relationship between $B^*_{C2}(0,\varepsilon_I)$ and $T^*_C(\varepsilon_I)$ with a typical value of ~2.2 for the exponent. Both results differ from those obtained previously for binary, low-upper-critical-field (~24 T) Nb_3Sn wires in which $B^*_{C2}(0)$ and T^*_C are less strain-dependent and the power-law exponent is larger (≥ 3).

The standard Summers Scaling Law therefore provides a relatively weak strain-dependence for J_C which does not accurately fit the $J_C(B,T,\varepsilon)$ data for either the EM-LMI or Vac wires.

We derive a simplified Interpolative Scaling Law to describe $J_C(B,T,\varepsilon)$ in technological Nb_3Sn wires with high values of upper critical field, motivated by microscopic theory and scaling considerations. The scaling law incorporates a polynomial function for normalised $B^*_{C2}(0,\varepsilon_I)$ and modified power-law relations between the strain-dependent variables. It allows accurate (~4%) parameterisations to be made of complete $J_C(B,T,\varepsilon)$ datasets and, with appropriate universal values for some of the parameters, reasonably accurate and extensive predictions to be made from partial datasets.

Table of contents

1 Background and Introduction

The ITER model coils provide large scale integrated tests of high current (40–60 kA) cable-in-conduit superconductors in multi turn high field coils, under stress/strain conditions similar to those required in ITER. The Toroidal Field Model Coil (TFMC), with EM-LMI internal-tin Nb_3Sn wires in a stainless-steel jacketed cable, and the Central Solenoid Model Coil (CSMC), with Vacuumschmelze bronze-route Nb_3Sn wires in an Incoloy-908 jacketed cable[3]. On both coils, current sharing measurements can be performed on the conductors in the temperature range from 4.5–8 K for fields up to 9 T (TFMC) and over 13 T (CSMC). The CSMC coil has been successfully built and tested with two insert coils (CS and TF inserts). The TFMC has been tested in the TOSCA facility at FzK in Karlsruhe. The strain tolerance of the critical current of strands is an important engineering design parameter for such model coils. During construction of magnets, a wind–heat-treat–insulate–impregnate procedure subjects the conductor to limited elastic deformation. During cool-down, the differential thermal contraction of the different component parts in the system strains the conductor. In these model coils, the differential thermal contraction during cool-down causes intrinsic axial strains on the Nb_3Sn filaments of approximately −0.65% (compression) for the TFMC[4] and −0.3% for the CSMC[5], while the magnetic (operating) strains are ~0.1% (tension)[3] and occur cyclically.

In our previous contract (EFDA 02-662), the performance of the LMI and Vac strands were investigated under cyclic tests within a limited range of intrinsic strain ($\varepsilon_I \approx 0.7\%$), temperature ($T = 4.2$ K) and magnetic field ($B = 7$–8 T). $J_C(B)$ measurements on the EM-LMI and Vac wires have been performed at a temperature of 4.2 K and zero applied strain[6,7], as a function of temperature at zero applied strain[8,9], as a function of axial strain at 4.2 K[10-12], and over a limited range of phase space as a function of axial strain and temperature[8,13,14]. In this report (and associated paper[15]), we present the results of full comprehensive, high-sensitivity ($10\ \mu Vm^{-1}$) measurements of $J_C(B,T,\varepsilon)$ for both of the wires used in the model coil tests.

The structure of this report is as follows: In section 2, we address the properties of the helical springs used to measure the effect of axial strain on the critical current density of superconducting wires. The complexity of the axial and radial strains is outlined. Relevant measurements are presented and analysed using FEA. We conclude with a description of the optimum design for the helical spring to obtain accurate and reliable strain measurements. In section 3, we develop a scaling law based on a theoretical analysis of the effect of strain which combines microscopic theory and phenomenological theory—it includes a review of the extensive experimental data now available. In particular, we provide a justification of a simplified scaling law which is used to parameterise the data presented for the Vac and LMI wires.

2 Properties of helical springs used to measure the effect of axial strain on the critical current density of superconducting wires

2.1 Review of the use of springs for measuring the strain-dependence of J_C

Measurements of the axial strain dependence of the critical current density in high magnetic fields provide important information on technological superconducting wires and tapes. The brittle superconductor Nb_3Sn, which is the focus of this report, has been studied most extensively[1,10,14-26], due to its importance in superconducting magnet technology and large sensitivity to the strains that occur in magnets due to differential thermal contraction and Lorentz forces. For future large-scale and high-field applications of Nb_3Sn (e.g. ITER), quantifying the effect of axial strain (ε) on the critical current density (J_C) is particularly important[3,25]. Axial strain effects have also been investigated in a number of other materials including NbTi[27], Nb_3Al[2,28-30], $PbMo_6S_8$[31,32], MgB_2[17,33,34], Bi-2223[17,18,35-39] and YBCO[40]. In these measurements, the techniques used to apply the strain generally fall into one of two categories: "axial-pull" or "bending spring". In the axial-pull technique[1,10,41], strain is applied to a short straight sample via end-grips which also serve as the current leads. In the bending-spring technique, the conductor is attached to a thick spring which is then deformed to apply the strain to the sample. Various different spring geometries are used, including the helical ("Walters") spring[18,19,42], which is investigated in this section and is used for the measurements in this report, the U-shaped spring[14,17,34], and the arc-shaped ("Pacman") spring[17,43].

In standard J_C measurements, the conductor is perpendicular to the applied magnetic field (or to within ~6°)[26,44]. For axial-pull apparatus used in standard solenoid magnets, the sample length is therefore limited to the diameter of the cold bore: typically 40 mm[1]. U-shaped bending springs generally have a similar sample length[17]. In these short-sample measurements, the current-transfer regions near the current contacts can overlap with the region between the voltage taps, resulting in a current-transfer voltage being measured, which must be corrected for in order to obtain the intrinsic voltage-current characteristics[45,46]. The electric field criteria used to define J_C are therefore relatively high: typically 200–500 μVm^{-1}[1,14,45]. Axial-pull apparatus can be used with split-pair magnets in order to increase the sample length to typically 180 mm, although the maximum fields of these magnets are generally lower than solenoid magnets (≤15 T)[10,41]. A recent variation of the U-shaped bending spring, the Pacman, uses an initially curved beam to increase the sample length to ~120 mm (the circumference of the magnet bore)[17,43]. The Walters spring has a helical sample geometry similar to that used in (internationally-agreed) standard J_C measurement techniques[19,47,48]. This geometry accommodates ~800 mm long samples[18,19,42], enabling critical current density measurements to be routinely performed with a sensitivity of 10 μVm^{-1} and, with care, at electric fields below 1 μVm^{-1}[49].

Axial-pull measurements are limited to tensile applied strains, as samples generally buckle in compression. However, differential thermal expansion of the component parts of the conductor often leads to a compressive prestrain on the superconducting material, which makes measurements possible over a limited range of compressive intrinsic

strain[20,24,39]. The prestrain can in principle be increased by cladding the conductor in a stainless-steel jacket[50,51] or using specially-prepared wires[24]. In contrast, bending-spring measurements enable both compressive and tensile axial strains to be applied to a sample that is attached to the spring. These measurements are particularly important for predicting conductor performance in systems where the structural materials cause a large thermal precompression, such as the cable-in-conduit conductors with stainless-steel jackets used for fusion applications (see Section 3)[4]. In bending-spring measurements, differential thermal contraction of the spring and attached sample results in thermal stresses on the sample at cryogenic temperatures (in contrast to axial-pull measurements, in which there are no thermal stresses). For measurements on wires, it is generally assumed that the effect of the differential thermal contraction is simply to produce an additional axial strain on the conductor that can be subtracted in order to obtain the intrinsic strain behaviour—this assumption is confirmed in this report. Methods for estimating the thermal strain due to the sample holder have been described[18]. In addition, when strain is applied using a bending spring, there is both a transverse strain gradient across the width of the conductor (which depends on the cross-section of the turns of the spring[8,19]) and a longitudinal strain variation along the length of the conductor (see Section 2.4.3). Bending springs avoid the possibility of stress concentrations at weak points in the conductor, but the elasticity of the spring is also an issue. It is clear that the properties of the spring are important factors that must be understood in order to perform accurate variable-strain measurements on conductors. Detailed tests are reported here of the effects of spring material and geometry since although some such results have been presented for other types of bending springs[43], the results reported in the literature for helical springs are very limited.

In this section (and associated paper[52]), we present J_C versus axial strain data for LMI and Vac Nb_3Sn wires measured on helical springs of different materials and geometries, together with results from finite element analysis (FEA) of these systems. The influence of thermal prestrain, elasticity of the spring, and the transverse and

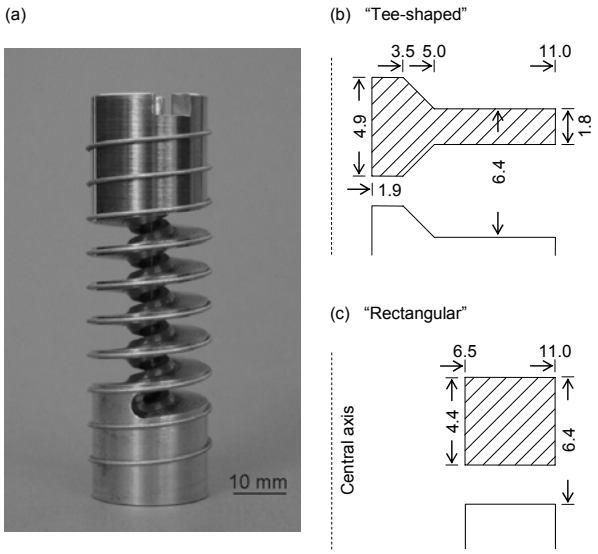

Figure 2.1. (a) Photograph of a superconducting wire mounted on a tee-shaped spring; (b) and (c) sections through turns of the tee-shaped and rectangular springs showing radial and axial dimensions in mm.

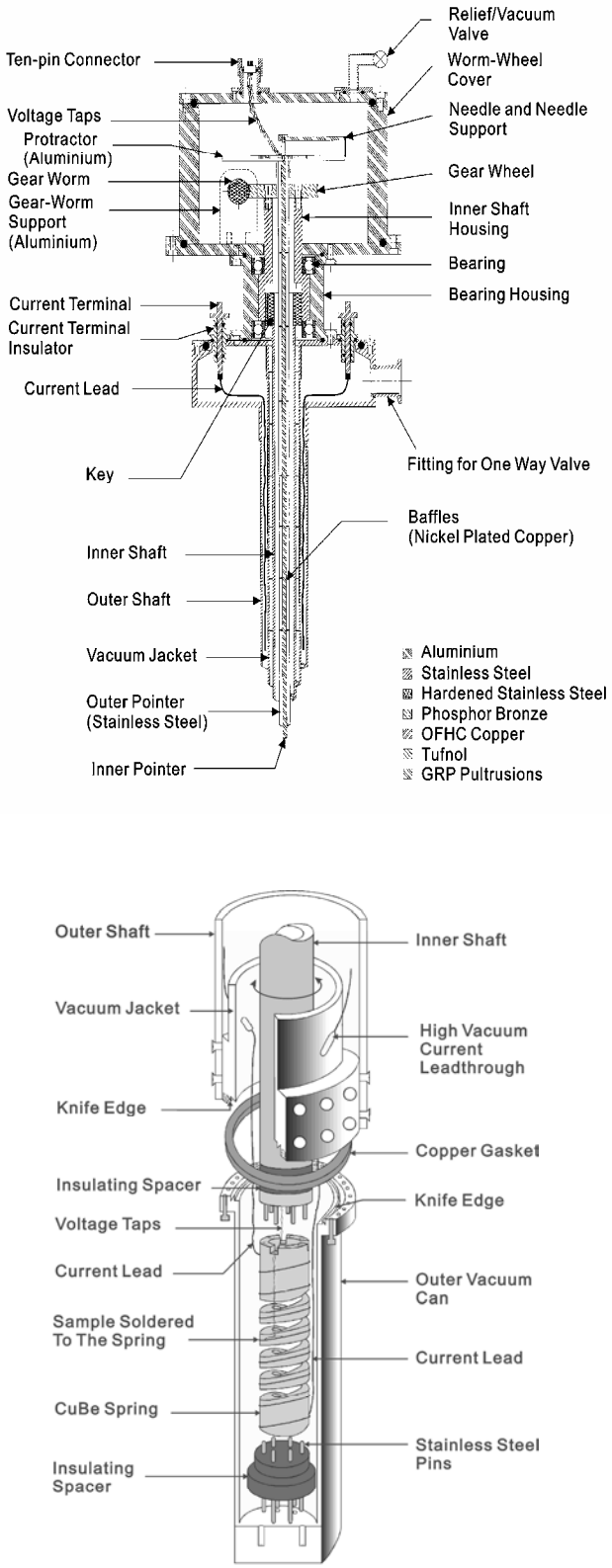

Figure 2.2. Schematic diagrams of the top and bottom parts of the $J_{\mathrm{C}}(B,T,\varepsilon)$ probe (reproduced from Cheggour and Hampshire[42]).

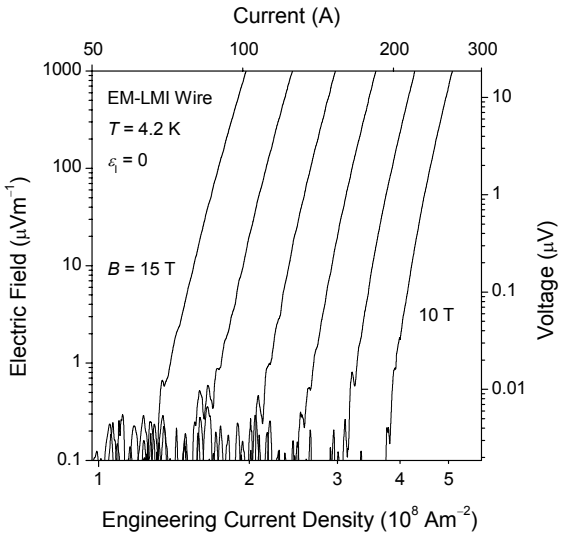

Figure 2.3. Log-log plot of electric field versus engineering current density (and voltage versus current) for the EM-LMI wire at a temperature of 4.2 K, zero intrinsic strain, and integer magnetic fields between 10 and 15 T.

longitudinal strain uniformity will be investigated in detail. We will evaluate the extent to which the intrinsic properties of conductors can be accurately measured (and hence to what degree the different measurement techniques are, in principle, equivalent[24,51]). Based on our experimental and FEA results, we will also report a number of recommendations about the design of helical springs, supplementing previous work by Walters *et al.*[19]. The section is organised as follows: Section 2.2 consists of a description of the apparatus and techniques, and the Vac and LMI samples investigated; the results of the variable-strain critical current density measurements are presented in Section 0; in Section 2.4, the FEA results are presented and comparisons are made with the experimental data; finally, some recommendations on spring design are made in Section 2.5.

2.2 Experimental procedure

2.2.1 Apparatus and techniques

$J_C(B,T,\varepsilon)$ measurements were performed on superconducting wires attached to helical springs [see Figure 2.1(a)] in which the strain is generated by rotating one end of the spring with respect to the other[19]. The probe (see Figure 2.2)[28,42] uses two concentric shafts to apply the torque to the spring: the inner shaft connects a worm-wheel system at the top of the probe to the top of the spring, and the outer shaft is connected to the bottom of the spring via an outer can. For measurements at 4.2 K, the outer can contains a number of holes to admit liquid helium from the surrounding bath, whereas for variable-temperature measurements, the outer can forms a vacuum space around the sample with a copper gasket and knife edge seal between the can and the outer shaft. The current leads sit in liquid or gaseous helium for the length of the probe, and enter the vacuum space around the sample via high-current lead-throughs[53]. At particular values of magnetic field, temperature, and strain, measurements are made of the voltage (V) across sections of the wire as a function of the current (I), which is increased at a constant slow rate.

Table 2.1. Range and uncertainty of the experimental parameters for the $J_C(B,T,\varepsilon)$ measurements.

Parameter	Range	Uncertainty
Voltage (Electric field)	≤50 μV (2500 μVm^{-1})	5 nV noise (Durham) (0.25 μVm^{-1})
Current	≤400 A (liquid He) ≤200 A (>4.2 K)	10 mA (≤120 A) 2 A (≤500 A)
Magnetic field	≤28 T (Grenoble) ≤15 T (Durham)	0.5%
Temperature	4.2 to 20 K	20 mK
Applied Strain	+0.7% to –2% ~10^3 cycles	3%

A number of modifications to the apparatus have been carried out to increase the range and accuracy of the various experimental parameters (see Table 2.1):

Voltage: In order to reduce thermal emfs, the copper voltage leads are continuous from the sample to the voltage amplifiers (except for a set of soldered joints close to the sample, where the temperature is approximately uniform). Measurements are performed using a nanovolt amplifier (EM-Electronics A10), the accuracy of which was checked against a nanovoltmeter (Keithley 182). The amplifier has a voltage noise equivalent to the Johnson noise of a 20 Ω resistor at room temperature. For a bandwidth of ~1.5 Hz, the expected noise is therefore ~2 nV (half the peak-to-peak value), or ~0.1 μVm^{-1} for the typical voltage-tap separation of 20 mm[54]. Figure 2.3 shows a representative set of *V–I* (or *E–J*: electric field–current density) characteristics, where a thermal offset voltage that is a linear function of current (time) has been subtracted from the measured data (typically 1 nV per 100 A): it can be seen that the noise floor is within a factor of ~2 of the amplifier noise. Voltages (electric fields) up to a maximum of ~50 μV (2500 μVm^{-1}) are generally measured, and up to three sections of the wire can be measured simultaneously.

Current: The total cross-sectional area of copper wire has been increased considerably in the vacuum space at the bottom of the probe (factor ~10) to reduce the ohmic heating in this region. In addition, the copper plating on the top and bottom parts of the spring (i.e. in the current transfer regions) is made particularly thick (up to ~1 mm), and the electrical contact between the current leads and the superconducting wire are made using this electroplated copper (the solder is applied subsequently). The maximum current that can be applied without heating of the sample is ~400A for measurements at 4.2 K, and ~200 A above 4.2 K. The uncertainty in the current is estimated to be 10 mA for our 120 A power supply, and 2 A for our 500 A supply.

Magnetic Field: Measurements in Durham are performed using our superconducting magnet in fields up to 15 T. An extended vacuum can and inner shaft (~600 mm long) also enable the probe to be used in a tail-dewar with a 38 mm diameter bore in magnetic fields up to 28 T using the resistive magnets at the European high-field laboratory (Grenoble). The field variation over the turns of the spring in both configurations is always less than 0.5%.

Temperature: Measurements above 4.2 K are carried out (in a low-pressure helium gas environment) using three independent temperature controllers with Cernox thermometers and constantan wire heaters distributed to produce a uniform temperature profile along the turns of the spring. The thermometers were calibrated commercially in zero magnetic field, and corrected for the small in-field changes to the calibration. The results of various consistency tests show that the uncertainty in the temperature of the wire is ~20 mK[15,28].

Strain: The uncertainty in the applied strain is estimated to be ~3% from a consideration of uncertainties in the calibration factors obtained from strain-gauge measurements, the correction factors used to calculate the strain at the middle of the wire, and the longitudinal strain variations. These factors are discussed below.

2.2.2 Samples

Measurements were made on the two ITER-candidate ∅0.81 mm Nb_3Sn wires: the EM-LMI internal tin wire and the Vacuumschmelze (Vac) bronze-route wire. The wires were heat-treated in an argon atmosphere on oxidised stainless-steel mandrels using a three-zone furnace (large isothermal zone), with an additional thermocouple positioned

Table 2.2. Properties of the different spring materials and of a typical Nb_3Sn wire.

Material	Thermal expansion 293–4 K (%)	Young's modulus at 4 K [293 K] (GPa)	Poisson's ratio at 4 K [293 K]	Elastic limit at 4 K [293 K] (%)
Titanium -4Al-6V	–0.174[a]	130[b] [110]	[0.31][b]	1.3[c] [1.0][d]
Copper-beryllium (TH04)	–0.317[a]	132 [119][c]	[0.27][b]	1.0 [0.9][c]
Brass (C27200)	–0.370[e]	[105][f]	[0.34][f]	[0.4][f]
Stainless steel 316L	–0.300[a]	208[a] [193[f]]	0.28 [0.29][g]	[0.1][f]
Nb_3Sn wire	–0.28[g,h]	25–100[g,i]	—	~0 [~0][g]
Copper	–0.334[g]	137 [128][g]	[0.31][f]	0.04 [0.02][g]
Nb_3Sn	–0.16[j]	100 [135][g]	0.4[j]	—

[a] Reference[55]. Stainless steel data is for type 316.
[b] Reference[56]. Cryogenic data for Ti-6Al-4V at 20 K.
[c] Reference[19].
[d] Reference[42].
[e] Reference[57]. 70/30 Brass (C26000).
[f] Reference[58].
[g] Reference[59]. Stainless steel data is for type 316LN.
[h] Reference[60]. Vacuumschmelze bronze-route wire.
[i] Reference[61]. A range of tangent modulus values are shown for the Nb_3Sn wire (which behaves plastically). Similar at 293 and 7 K.
[j] Reference[22].

next to the samples in order to monitor the temperature. The heat-treatment schedules were as follows: for the EM-LMI wire, 210°C for 100 h, 340°C for 24 h, 450°C for 18 h, and 650°C for 200 h (ramp rate: 50°C per hour throughout); for the Vac wire, 570°C for 220 h, and 650°C for 175 h (ramp rates: 100°C per hour, 80°C per hour, 100°C per hour). The wires were then etched in hydrochloric acid to remove the chromium plating, transferred to the springs, and attached by copper-plating and soldering (the Ti-6Al-4V spring was nickel-plated prior to attaching the wire). Two different geometries of spring were used for the measurements, details of which are given in Figure 2.1: the first (an older design) has turns with a rectangular cross-section, while the second uses a tee-

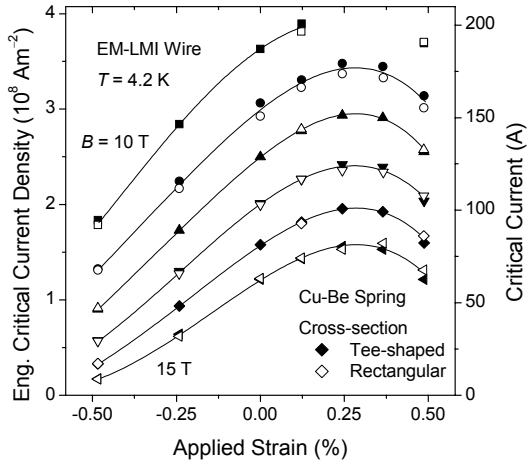

Figure 2.4. Engineering critical current density (and critical current) as a function of applied strain at 4.2 K and integer magnetic fields between 10 and 15 T. Data are shown for EM-LMI wires on Cu-Be springs with rectangular and tee-shaped cross-sections. The lines are a guide to the eye.

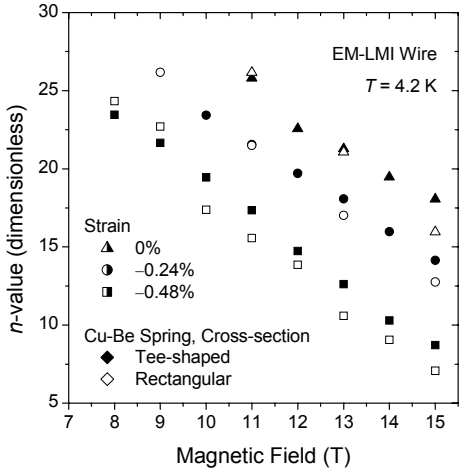

Figure 2.5. The *n*-value as a function of magnetic field at different applied strains at 4.2 K for EM-LMI wires on Cu-Be springs with rectangular and tee-shaped cross-sections.

shaped cross-section (based on the design of Walters *et al.*[19]). Measurements were performed on springs made from a number of different materials: Ti-6Al-4V, copper-beryllium (TH04 temper), brass, and stainless steel (SS) 316L. Table 2.2 shows some of the properties of these materials. Four EM-LMI samples were measured on rectangular springs made from the different materials, and a fifth EM-LMI sample was measured on a tee-shaped spring made from Cu-Be. In addition, Vac samples were measured on a brass rectangular spring and on a Cu-Be tee-shaped spring. Variable-strain J_C measurements were carried out at 4.2 K in magnetic fields up to 23 T in Grenoble (expect for the EM-LMI sample on the Cu-Be tee-shaped spring, which was measured in magnetic fields up to 15 T in our superconducting magnet). In all of the measurements, tensile strains were first applied to the sample and then compressive strains. J_C at zero applied strain was generally found to be reversible after the tensile strain cycle to within ~1%, in agreement with previous strain cycling results[12,62].

Engineering critical current density (J_C) data were calculated by dividing the critical current (I_C) by the total cross-sectional area of the wire (5.153×10^{-7} m^2) and defined at an electric-field criterion of 10 μVm^{-1}. J_C was calculated using the value of current in the superconducting material alone, obtained by subtracting the current in the normal shunt from the total current (for example, the typical shunt resistance is ~5 μΩ at 6 T corresponding to a shunt current of 40 mA at 10 μVm^{-1})[28].

2.3 Critical current versus strain results

2.3.1 Results for different spring geometries

Figures 2.4 and 2.5 show variable-strain engineering critical current density and *n*-value data for EM-LMI wires mounted on Cu-Be springs with rectangular and tee-shaped cross-sections. The *n*-value is calculated using $E \propto J^n$ for electric fields between 10 and 100 μVm^{-1}. The applied strains are calculated using calibration data from strain gauges mounted on the surface of the spring that are corrected using FEA to give the strain at the

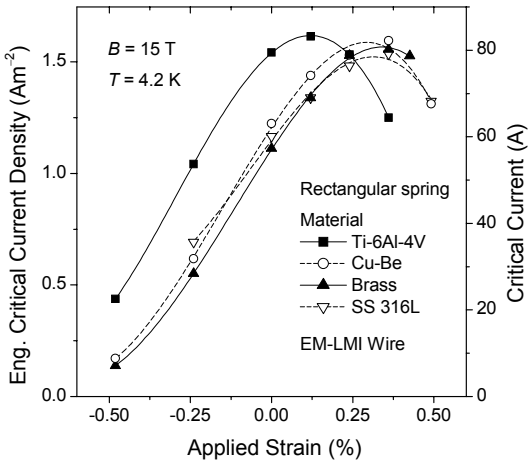

Figure 2.6. Engineering critical current density (and critical current) at 15 T and 4.2 K as a function of applied strain for EM-LMI wires on rectangular springs made from four different materials. The lines are a guide to the eye.

midpoint of the wires as described in Section 2.4.1. Good agreement is found between the results for the two different spring geometries (i.e. the old rectangular spring geometry reported in EFDA02-662 and the new tee-piece shaped springs reported) when the applied strain is FEA-corrected to account for the strain gradient across the wire: the J_C data superimpose to within ±2%, and the *n*-value data to within ±10%. These results therefore validate the methods used to obtain the characteristic strain for the wire (see Section 2.4.1).

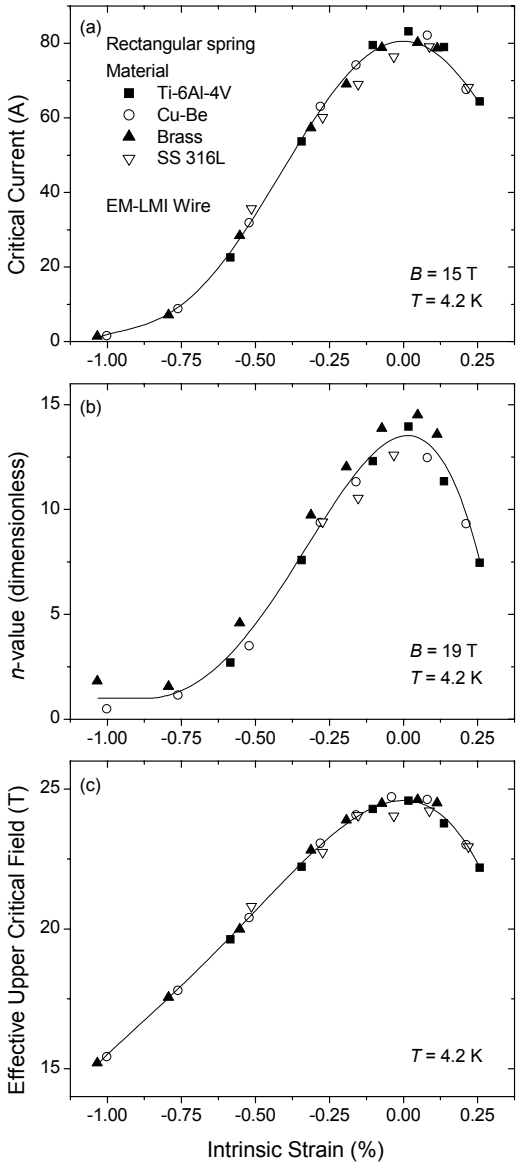

Figure 2.7. (a) Critical current at 4.2 K and 15 T, (b) *n*-value at 4.2 K and 19 T, and (c) effective upper critical field at 4.2 K as a function of intrinsic strain for EM-LMI wires on four different spring materials. The lines are a guide to the eye. Intrinsic strain was calculated from the applied strain by subtracting the value at which the effective upper critical field is a maximum.

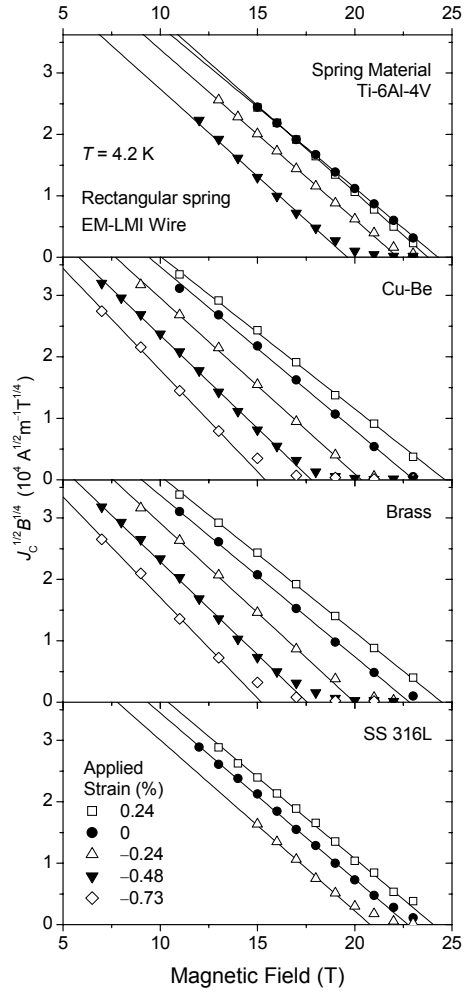

Figure 2.8. Kramer plots at different applied strains at 4.2 K for EM-LMI wires on rectangular springs made from four different materials.

2.3.2 Results for different spring materials

Figure 2.6 shows the engineering critical current density as a function of applied strain (ε_A) for EM-LMI wires on rectangular springs made from four different materials—reported in EFDA02-662 and FEA corrected. The spring material clearly affects the relationship between J_C and applied strain, and in particular the position of the peaks in $J_C(\varepsilon_A)$. Intrinsic strain (ε_I) is defined relative to the applied strain where J_C is a maximum (ε_M) by:

$$\varepsilon_I = \varepsilon_A - \varepsilon_M . \tag{0.1}$$

It is found by plotting J_C as a function of intrinsic strain, that the data for the four different spring materials approximately superimpose, typically to within ±5% [see Figure 2.7(a)]. Similar agreement is also found for the *n*-value [Figure 2.7(b)] and the

effective upper critical field [Figure 2.7(c)]. The values of effective upper critical field Figure 2.7(a)]. Similar agreement is also found for the *n*-value [Figure 2.7(b)] and the effective upper critical field [Figure 2.7(c)]. The values of effective upper critical field [$B^*_{C2}(4.2\ \mathrm{K})$] were obtained from Kramer plots, examples of which are shown in Figure 2.8[64]. The level of agreement between the different samples is typically ±1% for the $B^*_{C2}(4.2\ \mathrm{K})$ data as a function of intrinsic strain. The largest deviations from the universal curves are observed for the stainless steel spring. This can be attributed to

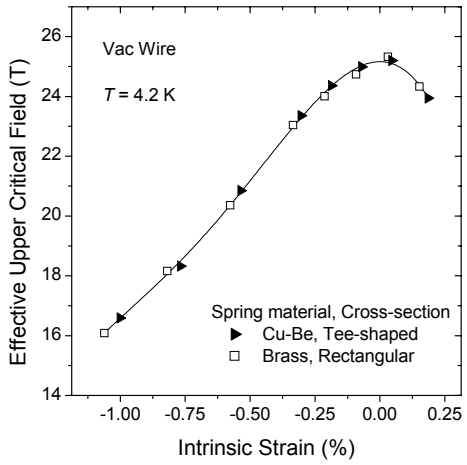

Figure 2.9. Effective upper critical field at 4.2 K as a function of intrinsic strain for Vac wires on springs of different materials and cross-sections. The line is a guide to the eye.

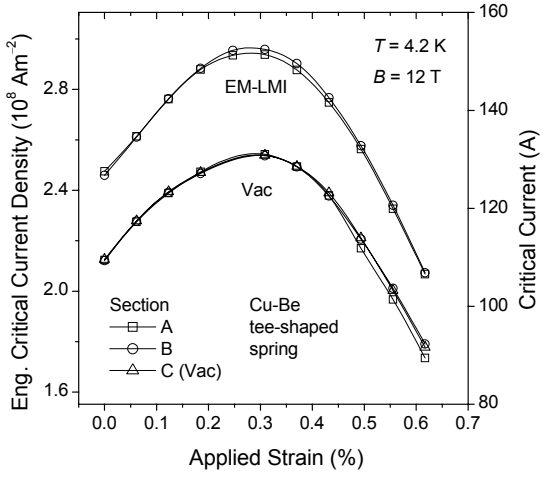

Figure 2.10. Engineering critical current density (and critical current) as a function of applied strain at 12 T and 4.2 K for three different sections of a Vac sample and two different sections of an EM-LMI sample, both on Cu-Be tee-shaped springs. The lines are a guide to the eye.

plastic yielding of the steel, which has an elastic limit of ~0.1%, and difficulty bonding the wire to the spring. The different values of ε_M are related to the additional thermal strains due to the sample holder, which vary according to the thermal expansion of the material used (see Table 2.2). The universal intrinsic strain dependences show that these additional strains are predominantly axial in nature, so that the same strain-state in the wire is obtained from different combinations of applied (mechanical) strain and thermal strain. In Section 2.4.2, the measured values of ε_M will be compared with predictions from FEA.

Figure 2.9 shows the values of effective upper critical field at 4.2 K obtained from measurements on Vac wires mounted on springs of different materials and geometries (a brass rectangular spring and new data on a Cu-Be tee-shaped spring). These data also lie on a universal curve as a function of intrinsic strain to within ±1%.

2.3.3 J_C homogeneity along the wire's length

Figure 2.10 shows the strain-dependence of J_C for different sections of Vac and EM-LMI samples on Cu-Be tee-shaped springs. Each section was ~20 mm long and separated by approximately one turn. The J_C data agree to within ±2% for both samples, which is typical of the samples that we have investigated, although occasionally (one in fifteen samples) significantly different behaviour is observed for one of the sections of the wire[42].

2.4 Modelling results and comparisons with experimental data

2.4.1 Results for different spring geometries

2.4.1.1 Analytic equations Walters *et al*. gives the following expression for the circumferential strain $\varepsilon_{\theta\theta}$ in a helical bending spring as a function of the radial distance r[19]:

$$\varepsilon_{\theta\theta} = K\left(1 - r_n / r\right), \tag{0.2}$$

where K is a factor that depends on the applied angular displacement θ, the number of turns of the spring N, and the pitch angle α:

$$K = \left(\theta / 2\pi N\right)\cos\alpha\,. \tag{0.3}$$

The position of the neutral radius r_n can be calculated using the condition that there is no net force perpendicular to the cross-section of the spring, i.e.:

$$\int w(r)\,E(r)\,\varepsilon(r)\,\mathrm{d}r = 0\,, \tag{0.4}$$

where w is the width of the section (in the axial direction) and E is the Young's modulus (both of these quantities can vary with position to allow for complex spring geometries and the presence of the wire—the integral can generally be calculated analytically). Equations (0.2)–(0.4) can be used to predict the strain-state in springs and attached wires, although the treatment does not consider the effects of the complex distortions that occur

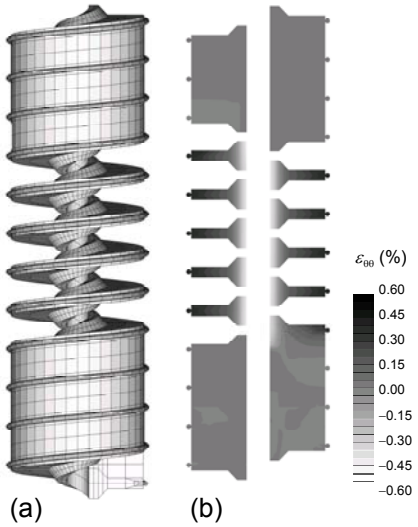

Figure 2.12. (a) FEA model of a tee-shaped spring with attached wire. (b) The circumferential strain on a plane through the centre of the spring at an angular displacement of +15°.

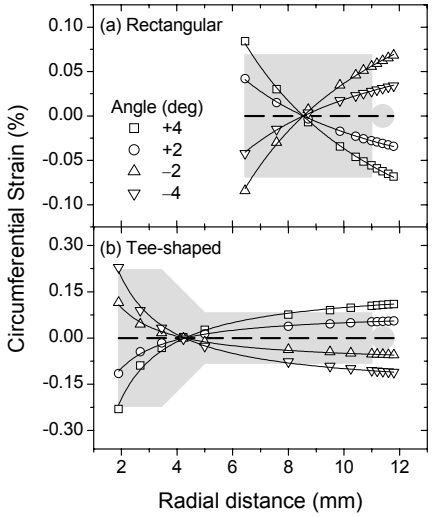

Figure 2.11. The circumferential strain as a function of the radial distance at different angular displacements for (a) rectangular and (b) tee-shaped springs with attached ∅0.81 mm wires. The symbols show the FEA results at the centre of the cross-section (shown by the dashed lines), while the solid lines show fits made using Equation (0.2). The variation in strain in the axial direction is negligible (see Figure 2.12).

when the spring is twisted[19]. These "loaded beam" equations will be compared with results obtained from finite element analysis in the next section.

2.4.1.2 Finite element analysis A typical finite element model consisting of ~20 000 8-node brick elements is shown in Figure 2.12(a). The results were found to change by less than 1% for further increases in mesh density. The models used elastic-plastic material properties with stress-strain curves defined via a modified power-law fit to the following parameters: Young's modulus, yield stress, ultimate stress, and elongation at

ultimate stress[59]. Figure 2.12(b) shows the circumferential strain due a +15° (anticlockwise) rotation of one end of the spring. The strain is approximately independent of axial position throughout the cross-section of a turn of the spring. The variation of circumferential strain with radial distance (along the centre of the cross-section) is shown in Figure 2.11 for the Cu-Be rectangular and tee-shaped springs used in the J_C vs. ε measurements. The FEA results can be fitted quite accurately using Equation (0.2) with r_n and K as free parameters (lines in Figure 2.11). The values of r_n obtained from the FEA (8.52±0.01 mm for the rectangular spring and 4.24±0.03 mm for the tee-shaped) agree well with those calculated using Equation (0.4) (8.54 and 4.24 mm). The two methods therefore give approximately the same radial-dependence for the strain in the turns, although not the same absolute values of strain (discussed below).

For the spring in the elastic regime, a linear relation between strain and angle is observed experimentally in strain-gauge calibrations, obtained from the finite element analysis (to within ~0.5%), and predicted by Equation (0.3). Table 2.3 shows calibration factors defined as the strain per unit angular displacement at various radial positions: the outer surface of the spring, the active part of a strain gauge (total height above the surface

Table 2.3. Calibration factors (% applied strain per degree angular displacement) for the Cu-Be rectangular and tee-shaped springs. Factors obtained from finite element analysis and the loaded-beam equations are shown for springs with and without attached wires (∅0.81 mm, $E = 30$ GPa), giving the strain at the outer surface of the spring, at the active part of a strain gauge (i.e. 45 μm above the surface of the spring) and at the middle of the wire. The corrected calibration factors (for the middle of the attached wire) are calculated from the measured values (for strain gauges on springs without attached wires) using the FEA results.

Cu-Be spring geometry	Position	Calibration factor (% per degree)			
		Measured	FEA	Loaded-beam eqs.	Corrected
		with shafts	no shafts	no shafts	with shafts
Rectangular					
No attached wire	Outside of spring		0.0143	0.0156	
	Strain gauge	0.0139	0.0145	0.0158	
Attached wire	Outside of spring		0.0141	0.0155	
	Middle of wire		0.0159 (+9.3%)	0.0174 (+10.1%)	0.0152
Tee-shaped					
No attached wire	Outside of spring		0.0269	0.0380	
	Strain gauge	0.0221	0.0269	0.0381	
Attached wire	Outside of spring		0.0267	0.0379	
	Middle of wire		0.0275 (+2.0%)	0.0388 (+1.7%)	0.0226

Table 2.4. Design parameters for the Cu-Be rectangular and tee-shaped springs, obtained both from FEA and the loaded-beam equations.

Cu-Be spring geometry	Strain gradient across ∅0.81mm wire (%)	Torque per % applied strain (Nm)	Ratio of strain at inside of spring to strain at outside of spring
	FEA [loaded-beam eqs.]		
Rectangular	±9.9 [±10.5]	27 [22]	–1.47 [–1.44]
Tee-shaped	±2.9 [±2.1]	67 [63]	–2.16 [–1.97]

of the spring: 45 μm[65]), and the midpoint of a ∅0.81 mm wire. Calibration factors are presented for strain-gauge measurements on springs without attached wires in the strain-probe (helical strain), finite element analysis (helical strain, averaged over the central turns of the spring: see Section 2.4.3), and the loaded-beam equations (circumferential strain). Helical strain is defined as the strain parallel to the helical path at a particular radius (e.g. the axis of the wire), and differs from the circumferential strain by typically 1% on the outer surface of the spring. The measured calibration factors are the lowest of the three, primarily because of the shafts and connectors twisting in the probe (the rotation of the top of the spring is measured directly, but, in standard operation, the rotation of the bottom of the spring is measured via the shafts and connectors that carry the torque). For the rectangular springs, there is reasonable agreement between the measured calibration factor and the value from FEA. The larger differences observed for the tee-shaped spring are consistent with the prediction that the torque required per unit angular displacement is a factor of ~4 larger for this spring (see Tables 2.3 and 2.4). The calibration factors from the loaded-beam equations are considerably larger than the FEA values, which can be attributed to the effects of the radial compression and the distortion of the envelope of the turns that occur when the spring is twisted: these effects are not included in the loaded-beam equations and are expected to reduce the strains relative to the calculated values[19]. Strain-gauge measurements show that the calibration factors are independent to within ~2% of both spring material and temperature (293–4 K), consistent with FEA and the loaded-beam equations for springs with and without attached wires.

The FEA results have been used to relate the measured calibration factors (for which the strain gauge is attached to the surface of a spring without an attached wire) to the strain at the midpoint of a ∅0.81 mm wire attached to the spring. For these wires, there is negligible difference between the calculated strain at the midpoint and the mean strain on the filaments. As shown in Table 2.3, the effect of attaching a wire ($E = 30$ GPa) to the spring decreases the calibration factor, whereas the radial-dependence of the strain and the different radial positions of the strain gauge and the midpoint of the wire cause the calibration factor to increase (see Figure 2.11). For the experimental data presented in this report, the strain values are always quoted for the midpoint of the wire using the corrected calibration factors. The FEA corrections are ~2% for the tee-shaped spring and ~9% for the rectangular spring, the magnitudes of which are confirmed by the loaded-beam equations. The good agreement between the results for different spring geometries demonstrates that this approach is valid (Figures 2.4, 2.5, and 2.9).

The transverse strain gradient across the wire differs considerably between the two spring geometries. The variations are approximately ±10% for the rectangular spring and ±3% for the tee-shaped spring (see Table 2.4), although these values are somewhat smaller over the central region of the wire occupied by the superconducting filaments (approximately ∅0.7 mm for the EM-LMI wire and ∅0.5 mm for the Vac wire[66]). For the EM-LMI wire on the rectangular spring, the variation in strain corresponds to a variation in $B^*_{C2}\left(4.2\ \mathrm{K}\right)$ of ±0.5 T at an applied strain of –0.5%, while for the tee-shaped spring the variation is ±0.1 T. The agreement in the *n*-values for the different spring geometries, as shown in Figure 2.5, is to be expected if the intrinsic variations in the superconducting properties—due to composition gradients, for example—are larger than those due to the strain gradient[67,68].

The data in Table 2.3 are valid for the elastic regime of the spring material, where critical current versus strain measurements are generally carried out. Table 2.4 shows the ratio of the circumferential strain at the inside of the spring to the circumferential strain at the outside of the spring for the two different geometries (see Figure 2.12). The magnitude of the strain is higher at the inner surface, and so the spring will yield first in this region. We note that finite element analysis shows that at the inner surface of the spring, the circumferential strain is significantly different from the helical strain but has a similar magnitude to the von Mises equivalent strain that is appropriate for considering plastic yielding[69]. For a spring made of Cu-Be (with an elastic limit of 1%), yielding occurs when the strain on the outer surface is ~0.5% for the tee-shaped cross-section and ~0.7% for the rectangular cross-section. Since some of the data presented in Section 0 were obtained at high compressive strains where parts of the spring are in the plastic regime, the possible effects of plasticity also need to be considered. In strain-gauge measurements performed at room temperature on the Cu-Be rectangular spring (and a Ti-6Al-4V tee-shaped spring), deviations from the linear relation between strain and angle observed for the elastic regime became significant (equal to +2%) at an applied strain of –1.5% (–0.9% for the Ti-6Al-4V tee-shaped spring). These results are consistent with FEA that includes the role of plasticity and confirms that yielding at the inner

Table 2.5. Calculated change in length between 293 and 4 K of the EM-LMI Nb_3Sn wire (∅0.81 mm, $E = 30$ GPa) on rectangular springs of different materials, and predicted and measured values of ε_M.

Spring material	Length change of wire 293–4 K (%)	ε_M (%)	
	FEA [force-balance eq.]	Predicted (FEA)	Measured
Titanium-4Al-6V	–0.184 [–0.174]	0.12	0.10 ±0.02
Copper-beryllium	–0.315 [–0.316]	0.255	0.28 ±0.02
Brass	–0.364 [–0.369]	0.30	0.31 ±0.02
Stainless steel 316L	–0.300 [–0.300]	0.24	(0.27 ±0.02)

surface does not have a very large effect on the average strain at the outer surface.

Finite element analysis provides useful information about the changes in the spring's dimensions when a torque is applied. At angular displacements corresponding to ±1% applied strain, the predicted change in the spring's height (from 75 mm) is ±0.5 mm for the rectangular spring and ±1 mm for the tee-shaped spring. Our strain probe has a sliding keyway in the inner shaft to accommodate this change. If the spring is constrained so that the ends cannot move vertically, the calibration factor is predicted to be somewhat larger (~0.5%) for the rectangular spring and considerably larger (~5%) for tee-shaped spring. In addition, the outer diameter increases at compressive applied strains: the maximum increases are 1.5 mm (rectangular) and 0.5 mm (tee-shaped) at −1% strain (similar decreases occur for the inner diameter at tensile applied strains).

2.4.2 Results for different spring materials

It is well known that at cryogenic temperatures the filaments in a Nb_3Sn wire are under compressive strain due to differential thermal contraction. It is generally assumed that the peak in the critical current density occurs when the applied axial strain cancels the axial component of this thermal strain[20-22]. Hence we can write down the following formula for the applied axial strain at the peak (ε_M) for our particular measurement procedure:

$$\varepsilon_M = -\left(\left(\frac{\Delta l}{l}\right)^{923-293\ \mathrm{K}}_{\text{Isolated wire}} + \left(\frac{\Delta l}{l}\right)^{293-4\ \mathrm{K}}_{\text{Wire on spring}} - \left(\frac{\Delta l}{l}\right)^{923-4\ \mathrm{K}}_{\text{Nb}_3\text{Sn compound}} \right). \tag{0.5}$$

The first term on the right-hand side of the equation is the relative change in length of the isolated wire on cooling from the reaction temperature (923 K) to room temperature (293 K), which has been calculated using finite element modelling to be –0.63% for the EM-LMI wire[59]. The second term is the relative change in length of the wire that has been attached to the spring at room temperature (by copper plating) and then cooled to

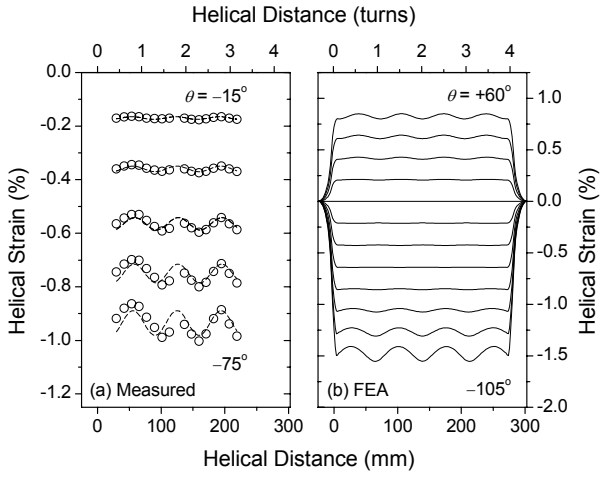

Figure 2.13. The helical strain at the outer surface of a Cu-Be rectangular spring (with four turns) as a function of helical distance: (a) results from strain-gauge measurements (the symbols show the measured data while the dashed lines are a guide to the eye); (b) finite element analysis results.

Table 2.6. The amplitude of the longitudinal strain oscillations for springs of different materials and geometries.

Spring material and geometry	Amplitude of oscillations (%)	
	–1.0% strain	+0.5% strain
Rectangular (N = 4)		
Cu-Be (meas.)	5	—
Cu-Be (FEA)	1.3	2.5
Brass (FEA)	3.9	3.6
Tee-shaped (FEA)		
Cu-Be (N = 4.5)	1.4	0.7
Cu-Be (N = 2, 3, 4, 5, 6)	2.6, 0.1, 0.25, 0.3, 0.35	—

4 K. A simple 1D "force balance" equation[39] gives values for the relative change in length of the wire between 293 and 4 K that are within ~1% of the thermal expansion of the spring material (compare Tables 2.2 and 2.5), due to the small cross-sectional area of the wire in relation to the spring. Similar values are obtained from FEA, although there are somewhat larger differences for the Ti-6Al-4V tee-shaped spring, where the average contraction of the wire is 5% higher than the thermal contraction of Ti-6Al-4V (see Table 2.5). The third term on the right-hand side of Equation (0.5) is the intrinsic thermal expansion of Nb_3Sn between 923 and 4 K, for which a value of –0.69% has been used (923–293 K: –0.53%, 293–4 K: –0.16%)[22]. Table 2.5 shows the values of ε_M calculated using Equation (0.5), which show good agreement with the experimentally measured values for the different spring materials.

Various studies have been carried out of the three-dimensional strain-state of the filaments in Nb_3Sn wires[70-75]. Given the uncertainties in some of the parameters used in Equation (0.5), our results are consistent with models in which the peak in the superconducting properties occurs when the deviatoric strain or the axial strain in the filaments is a minimum (zero). In any case, the FEA confirms that after cool-down, the 3D strain-state of the (EM-LMI) wire attached to the spring is, to a good approximation, equal to the strain-state of an isolated wire that is first cooled down and then subject to an axial strain. This equivalence between the thermal strains and the applied (mechanical) strains provides an explanation for the universal behaviour of the wires as a function of intrinsic strain (see Section 2.3.1). Note that this is not the case for tape conductors, where the differential thermal contraction also leads to an in-plane transverse strain on the tape[76] (or for a wire attached to the spring with large amounts of copper-plating or solder).

2.4.3 Strain uniformity along the wire's length

In order to investigate the uniformity of the strain along the length of the wire, measurements were carried out using 16 strain gauges placed around the outer surface of a Cu-Be rectangular spring. A sinusoidal variation of strain with helical distance was observed, as shown in Figure 2.13(a). The results obtained from the finite element analysis are shown in Figure 2.13(b). The measured "oscillations" have a similar wavelength to the FEA results (equal to one turn) but are both considerably larger and

off-set spatially. At a mean applied strain of −1%, the measured value for the amplitude is ~5% of the mean, compared to the FEA value of 1.3% (see Table 2.6).

Finite element analysis was used to investigate the strain variations for various types of spring over extended strain ranges. The size of the oscillations generally increases non-linearly with increasing strain, and for the Cu-Be rectangular spring is considerably larger at tensile strains than equivalent compressive strains, as shown in Figure 2.13(b). For the Cu-Be tee-shaped spring with four-and-a-half turns (used for the critical current measurements), the oscillations have a similar size to the rectangular spring in compression but are smaller in tension (see Table 2.6). Tee-shaped springs with integer number of turns ($N = 4$, 5 or 6) have considerably smaller oscillations, by a factor of ~5 at −1% strain, than the ($N = 4$) rectangular spring and the half-integer ($N = 4.5$) tee-shaped spring.

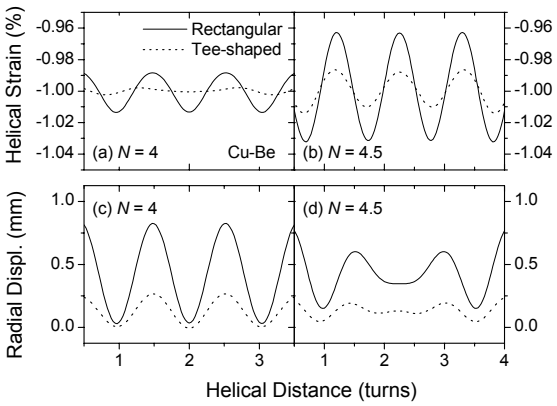

Figure 2.14. The helical strain and radial displacement at the outer surface of springs with 4 and 4.5 turns as a function of helical distance (results from FEA).

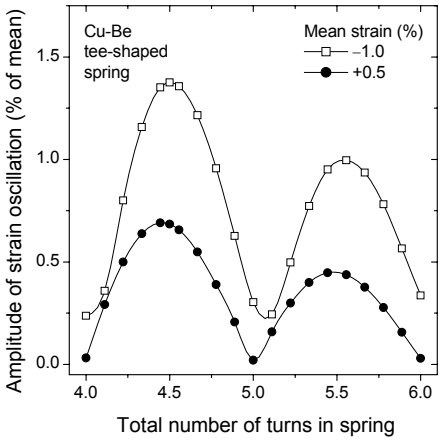

Figure 2.15. The amplitude of the longitudinal strain oscillation at −1% and +0.5% mean strain at the outer surface of a Cu-Be tee-shaped spring as a function of the total number of turns in the spring (results from FEA).

Finite element analysis shows that the strain oscillations are related to the distortion of the envelope of the turns that occurs when the spring is twisted. For springs with integer numbers of turns, a correlation is observed between strain magnitude and radial displacement as a function of helical distance [see Figures 2.14(a) and (c)], although for springs with half-integer number of turns, there is no simple correlation [Figures 2.14(b) and (d)]. The behaviour is clearly quite complex, and, to our knowledge, an analytic description is not yet available. The smaller oscillations for the tee-shaped springs can be attributed to the greater torsional rigidity of the cross-section and hence smaller distortions. Figure 2.15 shows how the oscillation amplitude varies as a function of the total number of turns in the Cu-Be tee-shaped spring at +0.5% and −1.0% strain. It can be seen that for this type of spring an integer number of turns (4 or 5) is indeed the optimum number for minimising the oscillations.

It was also found that the longitudinal oscillations are considerably larger when the spring material is in the plastic regime (presumably because the spring yields first at the peaks of the oscillations which therefore increase disproportionally). For example, a finite element model of a (brass) spring with an elastic limit of 0.4% (rather than 1.0% for Cu-Be) has oscillations that are larger by a factor of ~3 at −1% applied strain (see Table 2.6). Hence the difference between the experimental results and the FEA in Figure 2.13 may be partly due to the copper-beryllium used for the spring having a lower elastic limit than the typical value at room temperature (0.9%).

2.5 Discussion of spring design

Our experimental and FEA results allow us to make some recommendations about optimum spring designs. The universal relations between superconducting properties and intrinsic strain for wires on different spring materials demonstrate that the thermal expansion of the spring only affects the behaviour of wires through a change in the parameter ε_M. However, it is important to use a spring material with a high elastic limit—such as Cu-Be (TH04 temper) or Ti-6Al-4V—given the requirement for a reversible (unique) relationship between angular displacement and strain, the deviations observed for the J_C measurements on the stainless-steel spring, and the increase in the size of the longitudinal strain variations predicted by the FEA for springs in the plastic regime. We now prefer to use the titanium alloy, as it is routinely used for sample-holders in standard J_C measurements[8,9] and it has the highest elastic limit at 4.2 K of any engineering alloy (we have also used copper-beryllium, but the sensitivity to heat-treatment conditions and the toxicity of the beryllium means that some care is required when handling). Although Ti-6Al-4V cannot easily be soldered to or copper-plated directly, we have used a well-established technique for nickel plating the spring[77] prior to transferring and attaching the wire using copper-plating and soldering.

The J_C data demonstrate that it is necessary to use finite element analysis (or the loaded-beam equations) to relate the strain-gauge calibration data to the strain at the midpoint of the conductor. After applying the correction to obtain the strain at the middle of the wire, second-order effects due to the different strain gradients for the two spring geometries are not observed for our results. The magnitude of the strain gradient may be important for larger or different types of conductor, and can be reduced by using a spring with a radially thicker, tee-shaped cross-section (our optimised tee-shaped springs have strain gradients and correction factors of <3%). As the radial thickness of the spring is increased, the ratio of the strain at the inside of the spring to the strain at the outside increases in magnitude, reducing the strain range over which the spring remains elastic.

Walters *et al.* suggested maximising the elastic strain range by setting this ratio to be equal to -1[19]. We have used an alternative approach in which the value of the inner/outer strain ratio is specified by the strain range over which measurements are required, and then the tee shape is optimised to minimise the strain gradient across the conductor. Our specific requirements are for detailed measurements to ±0.5% applied strain and hence for a spring material with an elastic limit of ~1% we use an inner/outer strain ratio of –2. To optimise the properties of the spring, the loaded-beam equations given by Walters *et al.* can be used (see Section 2.4.1.1), as these predict a radial-dependence for the strain in the turns that agrees well with the FEA[19]. The first stage of the process is the same as that described by Walters *et al.* and involves maximising the outer radius of the spring (given the available space), minimising the width at the outside of the tee (given the width of the conductor), and maximising the width at the inside of the tee (given the maximum pitch-angle for the wire of ~5°[44] and hence the turn pitch)[19]. The two parameters to be calculated are then the inner radius and the position of the ramped step (see Figure 2.1). For any given value of inner radius there is an optimum step position that minimises the neutral radius [calculated using Equation (0.4)] and hence minimises both the strain gradient across the conductor and the size of the inner/outer strain ratio [Equation (0.2)]. The optimum step position can be calculated at discrete values of inner radius using a spreadsheet solver/optimiser. Hence the optimum inner radius and ramped step position are uniquely determined once the inner/outer strain ratio is specified by the required elastic strain range.

The geometry of the tee-shaped spring used in our measurements [see Figure 2.1(b)] was obtained using the method described above with an inner/outer strain ratio of –2. For this spring, the loaded-beam equations predict a strain gradient across a ∅0.81 mm wire of ±2.1% (FEA: ±2.9%) compared to the value of approximately ±6% that would be obtained using the approach of Walters *et al*. The reversibility of the critical current density and strain-gauge calibration data also imply that measurements can generally be carried out on a single cycle to a value of compressive strain beyond the predicted elastic regime (by a factor of ~2). In general, the availability of a larger bore diameter enables both a larger strain range and a smaller strain gradient across the conductor.

The design should also consider the torque required to twist the spring, which can also be calculated using the loaded-beam equations, so that higher-strength shafts are used for springs with radially thicker turns[19,42]. The FEA results for the tee-shaped spring also show that the calibration factor is quite strongly dependent (~5%) on whether the height of the spring is able to change. Our probe is designed with a sliding keyway so that the change in height can occur freely (or, at least, reproducibly).

Finite element analysis shows that the uniformity of the strain along the length of the wire varies quite considerably with spring material and geometry. These longitudinal strain variations can be large, but our FEA results show that they can be reduced to <0.5% by using a spring with an optimum integer number of turns (4 or 5).

2.6 Conclusions

Variable-strain critical current density data and finite element analysis results are presented for Nb_3Sn wires on helical (Walters) springs of different materials and geometries. The strains produced by these springs can in principle be much more complex than those produced by axial pull techniques. For the Vac and LMI wires measured on different spring materials (Cu-Be, Ti-6Al-4V, brass, SS 316L), the critical current density, *n*-value, and effective upper critical field are universal functions of

intrinsic strain—deviations are observed for the stainless-steel spring which are attributed to plasticity. The experimental and modelling results demonstrate that the thermal strains due to the spring are predominantly axial in nature, so that the only effect on the behaviour of the wire is a change in the parameter ε_M, which depends systematically on the thermal expansion of the spring material. The variable-strain data obtained on different spring geometries show good agreement when the applied strain is calculated at the midpoint of the wire using strain-gauge calibration data corrected to account for the strain gradient across the wire (and the presence of the wire on the spring). The agreement is observed even though the transverse strain gradient for the rectangular-shaped spring used in our measurements is considerably larger than for the tee-shaped spring. The correction factors can be obtained from FEA or analytical calculations. Experimental results show that the critical current density is uniform along the length of the wire typically to within ±2%. Finite element analysis shows that the variations in strain along the length of the wire vary considerably with spring material and geometry, but are generally less than ±2% for our measurements. The universal strain dependences observed for different types of helical spring provide good evidence that the intrinsic properties of the conductor can be accurately measured—the capacity for very high-field and high-sensitivity measurements is also demonstrated. Supplementing previous work by Walters *et al.*, springs made with highly elastic materials (e.g. Ti-6Al-4V), optimised tee-shaped cross-sections, and optimum integer numbers of turns (e.g. 4 or 5) are shown to give the best performance in relation to the transverse and longitudinal strain uniformity in the wire.

3 Equation Chapter (Next) Section 1The scaling law for the strain-dependence of the critical current density in the Vac and LMI Nb_3Sn superconducting wires

3.1 Introduction to scaling laws

$J_C(B,T,\varepsilon)$ data are parameterised using scaling laws, which allow the interpolation and extrapolation of the measured data for interlaboratory comparisons and magnet design. A number of different empirical scaling laws have been proposed to describe the magnetic field, temperature, and axial strain-dependence of J_C in Nb_3Sn wires. These scaling laws generally incorporate aspects of the temperature scaling law of Fietz and Webb[78] (with subsequent refinements[79]) and the strain scaling law of Ekin[1]. The latter followed from the well-known measurements[1] of J_C for a number of technological Nb_3Sn wires as a function of magnetic field and axial strain at 4.2 K (previous variable-strain measurements were also reported by a number of authors[20,23,80-84]). Both scaling laws relate changes in J_C to changes in the upper critical field (B_{C2}), although a fundamental inconsistency implies that an additional strain-dependent parameter is required in order to unify the two laws[16,23]. Summers *et al.*[85] subsequently proposed such a unified scaling law, which also includes Ekin's universal relation for the normalised values of $B_{C2}(4.2\text{ K},\varepsilon)$ for binary Nb_3Sn wires, and a power-law relationship between $B_{C2}(4.2\text{ K},\varepsilon)$ and $T_C(\varepsilon)$ (the critical temperature)[1]. The Summers Scaling Law parameterised the data available at the time quite accurately (although detailed variable-temperature-and-strain J_C data had not yet been reported) and was subsequently adopted as the standard formulae for large-scale magnet design[86]. Although the strains in magnets are three-dimensional in nature, there is now reasonable consensus (despite some conflicting results in the literature on the effect of transverse stress) that in the reversible strain regime, uniaxial (deviatoric) strain—whether applied in the axial or transverse direction—is the most important strain component: its effects in Nb_3Sn are approximately an order-of-magnitude larger than hydrostatic strain[70,71,87-90].

More recently a number of laboratories have succeeded in obtaining $J_C(B,T,\varepsilon)$ data, and various alternative scaling laws have been proposed[8,14,16,28,70,91]. In Durham, a general scaling law for $J_C(B,T,\varepsilon)$, the Interpolative Scaling Law (ISL), has been shown to allow very accurate parameterisations of comprehensive data for Nb_3Al and Nb_3Sn wires[28,91]. The Interpolative Scaling Law uses general polynomial functions for the strain-dependent parameters, in contrast to the Summers Scaling Law. It therefore contains a relatively large number of free parameters and cannot generally be used to extrapolate beyond the measured regions of parameter space (e.g. the measured strain range). It is desirable, particularly for engineering purposes, to develop a scaling law with fewer free parameters that can be determined from a smaller $J_C(B,T,\varepsilon)$ dataset, allowing accurate predictions for J_C to be made in other regions of parameter space. In this section, we develop such a scaling law based on a theoretical analysis of the effect of strain using microscopic theory and a review of the extensive experimental data now available. In particular, we use microscopic theory[2,71,92-97] to analyse the relationship

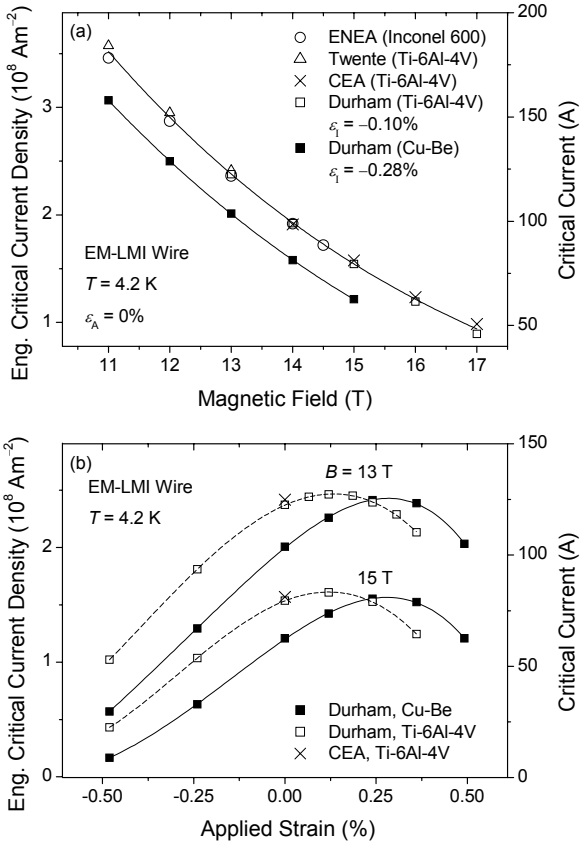

Figure 3.1. Interlaboratory comparisons for the EM-LMI wire: (a) Engineering critical current density (and critical current) at 10 μVm^{-1} as a function of magnetic field at 4.2 K and zero applied strain. (b) Engineering critical current density as a function of applied strain at 4.2 K, and 13 and 15 T. The data were obtained in Durham on Cu-Be and Ti-6Al-4V springs and in other laboratories on Ti-6Al-4V and Inconel-600 sample holders[7,9,13].

between $B_{C2}(0,\varepsilon)$ and $T_C(\varepsilon)$ (and the other strain-dependent parameters) and to help motivate the introduction of modified versions of the empirical power-law relations currently used[14,85]. A comparison of our theoretical and experimental results and the intension to derive a simplified scaling law means that we must address the question of whether the variations of the superconducting properties of Nb_3Sn with uniaxial strain are predominantly due to changes in the electronic or the phononic properties of the material[2,71].

The section is structured as follows: Sections 3.2 and 3.3 contain the main experimental results. Section 3.2 describes consistency tests and interlaboratory comparisons, and hence addresses how general and accurate the data are. Section 3.3 presents the $J_C(B,T,\varepsilon)$ data for the EM-LMI and Vac wires. These data are parameterised using the Interpolative Scaling Law and comparisons are made with alternative scaling laws. In Section 3.4, the observed relationships between $B_{C2}(0)$ and T_C are examined using microscopic theory. Finally, in Section 3.5, a new simplified Interpolative Scaling Law is presented. Its accuracy in parameterising complete datasets and extrapolating from partial datasets is demonstrated. The appendix provides a parameterisation of J_C data generated in Durham using this simplified law.

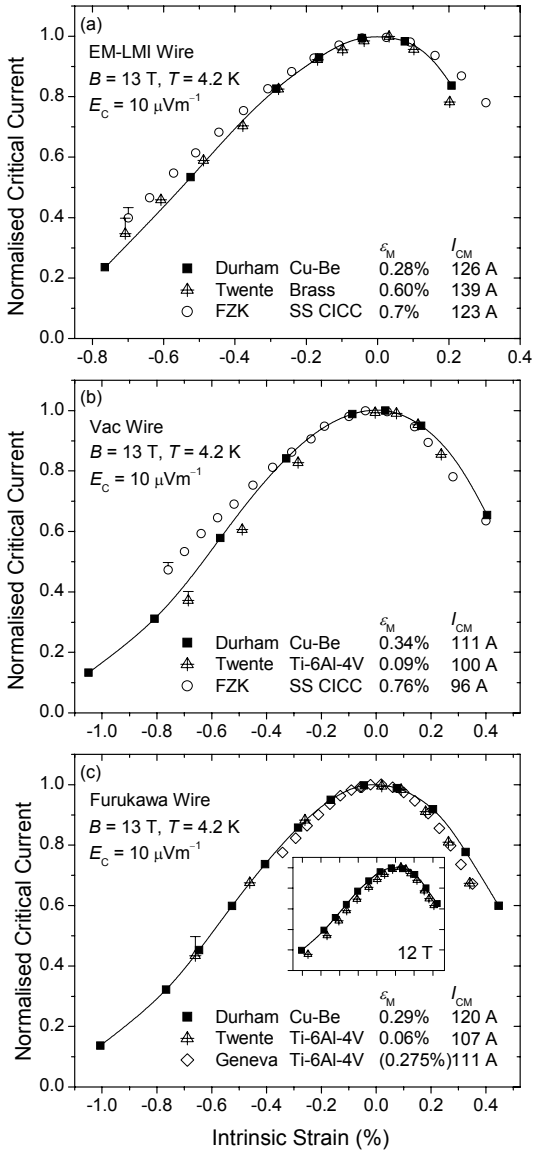

Figure 3.2. Interlaboratory comparisons of the normalised critical current as a function of intrinsic strain at 4.2 K and 13 T for (a) EM-LMI, (b) Vac and (c) Furukawa ITER Nb_3Sn wires. Critical currents were measured at 10 μVm^{-1} or calculated at 10 μVm^{-1} from measurements performed at higher electric-field criteria using *n*-values measured in Durham (the error bars show the effect of these calculations on the normalised values). The legends show the spring material (or the CICC jacket material), the value of applied strain where the critical current is a maximum (ε_M), and the value of the critical current at this maximum (I_{CM}). Inset (c): comparison of Durham and Twente Pacman data at 12 T (same axes and symbols as main graph)[8,10,11,13,18,98].

3.2 Consistency tests and interlaboratory comparisons

We will begin by presenting the results of various consistency tests and interlaboratory comparisons. These are vital given the complexities involved in making such measurements and the importance of the data for the ITER project, and enable the accuracy of the data to be addressed prior to comparison with theory.

3.2.1 Comparisons with other J_C data for as-prepared EM-LMI wires

Figure 3.1(a) shows the results of various measurements of the engineering critical current density of as-prepared EM-LMI wires as a function of magnetic field at 4.2 K[7,9,13]. In these (zero applied strain) measurements, the strain-state of the wire is determined primarily by the thermal expansion of the sample holder. It can be seen that the data from all of the laboratories agree to within ±2.5% for measurements on the same titanium alloy sample holder (as well as for an Inconel 600 sample holder) and hence show similar variations to those observed in the VAMAS international round-robin measurements[99]. Figure 3.1(b) shows our J_C data measured as a function of applied strain (ε_A) at 4.2 K for EM-LMI wires mounted on a Cu-Be spring and a Ti-6Al-4V spring. These data superimpose to within ~5% if plotted as a function of intrinsic strain (ε_I), where intrinsic strain is defined relative to the applied strain where J_C is a maximum (ε_M):

$$\varepsilon_I = \varepsilon_A - \varepsilon_M . \tag{1.1}$$

The values of ε_M are ~0.28% for the Cu-Be spring and ~0.10% for the Ti-6Al-4V spring, which are consistent with the thermal strain on the filaments due to the cool-down from 293 K (where the wire is copper-plated to the spring) to 4.2 K being determined by the thermal expansion of the spring material: –0.32% for Cu-Be and –0.17% for Ti-6Al-4V[100]. Therefore, as long as both the applied strains and the thermal strains are properly considered, the J_C datasets obtained on springs of different materials and geometry are consistent (see Section 2).

3.2.2 Comparisons of variable-strain J_C data for the EM-LMI, Vac, and Furukawa ITER wires

Interlaboratory comparisons of variable-strain J_C data for the EM-LMI and Vac ITER wires and cables are shown in Figure 3.2, where the normalised critical current at 4.2 K and 13 T is plotted as a function of intrinsic strain. Data are also shown for a Furukawa ITER Nb_3Sn wire[11]. The measurements in other laboratories were performed on individual wires at the University of Twente using different types of "bending spring"[8], at the University of Geneva using a helical spring[18], and on cable-in-conduit conductors at Forschungszentrum Karlsruhe (FZK) using an "axial pull" system[10]. Note that as J_C was measured at higher electric-field criteria at Twente (500 μVm^{-1}) and FZK (100 μVm^{-1}), we have calculated J_C at 10 μVm^{-1} from these data using n-values measured in Durham—n decreases by a factor of ~2 from 0% to –0.7% intrinsic strain so that the strain-dependence of the normalised critical current is larger at lower electric-field criteria. It can be seen that the agreement between the normalised critical current data from different laboratories is generally good. The biggest deviations occur for the

cable-in-conduit conductors at $\varepsilon_I \ll 0$, where the CICC data are less strain-sensitive. The normalised critical current data for measurements on wires agree to within ±6% for the EM-LMI wire ($\varepsilon_I = -0.7\%$), ±8% for the Vac wire ($\varepsilon_I = -0.7\%$), and ±2.5% for the Furukawa wire ($\varepsilon_I = +0.35\%$). We have particular confidence in our EM-LMI data because six different samples on springs of various materials and geometries all show a similar intrinsic strain-dependence for J_C to within ±5%, and the reversibility of J_C over a number of strain cycles (described below) demonstrates that the samples were not damaged. For all of the wires, there are variations of approximately ±7% between different laboratories for the value of the critical current at $\varepsilon_I = 0$, although some of these variations may be due to the different billets measured.

In general, obtaining reliable variable-strain J_C data presents a difficult experimental challenge. In addition to the standard good practice required for critical current measurements[63,99], there are a number of issues to be considered: damage to any part of the wire during mounting may have a considerable effect on the strain-dependence of J_C; the experimental set-up should preferably involve relatively long lengths of wire in a homogeneous strain-state beyond the measurement regions, in order to avoid current-transfer voltages[1,17]; and the sample holder (if used) should not be strained beyond its elastic limit. Plasticity of the component parts of the superconducting wires can also play a significant role in interlaboratory comparisons. In 3, measurements on EM-LMI and Vac wires demonstrated that extensive strain cycling can cause J_C to increase by up to ~7% at 4.2 K, 12 T, and $\varepsilon_I = 0$, without damaging the superconducting filaments[12]. These changes in J_C were attributed to changes in the radial stress on the filaments due to the plastic deformation of the matrix. In the present measurements, J_C for the EM-LMI wire (sample 1) at zero applied strain increased by ~3% after the cycle 0% → 0.49% → –0.48% → 0%, and J_C at –0.48% applied strain decreased by ~4% after the

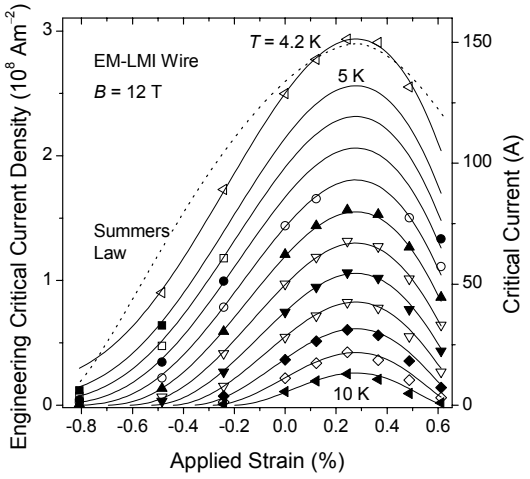

Figure 3.3. Engineering critical current density (and critical current) of the EM-LMI wire as a function of applied strain at 12 T and at 4.2 K and 0.5 K increments between 5 and 10 K. The symbols show the measured data, the solid lines the Interpolative Scaling Law, and the dotted line the Summers Scaling Law [obtained by fitting the $J_C(B,T,\varepsilon)$ data for $|\varepsilon_I| < 0.22\%$].

cycle –0.48% → 0.61% → –0.48%. Hence additional variations in the strain-dependence of J_C of the order of a few percent are to be expected when measurements at different laboratories involve multiple strain cycles (thermal or mechanical) that strain the wire beyond the elastic limit of the component materials (~0.1%). From a comparison of the variable-strain datasets available, we conclude that variations of typically ±5% in the strain-dependence of the normalised J_C can in principle be achieved between different laboratories.

3.3 $J_C(B,T,\varepsilon)$ scaling laws

3.3.1 Interpolative Scaling Law for $J_C(B,T,\varepsilon)$

The $J_C(B,T,\varepsilon)$ data can be parameterised using the Interpolative Scaling Law (ISL)[91] in which the volume pinning force ($F_P = J_C B$) is given by[101]:

$$F_P = \frac{A'(\varepsilon)\left[B^*_{C2}(T,\varepsilon)\right]^n}{\left[\kappa_1^*(T,\varepsilon)\right]^m} b^p (1-b)^q, \tag{1.2}$$

where $b = B/B^*_{C2}(T,\varepsilon)$ and $B^*_{C2}(T,\varepsilon)$ is the effective upper critical field which is parameterised by:

$$B^*_{C2}(T,\varepsilon) = B^*_{C2}(0,\varepsilon)\left(1-t^v\right). \tag{1.3}$$

Here, $t = T/T^*_C(\varepsilon)$ and $T^*_C(\varepsilon)$ is the effective critical temperature. $\kappa_1^*(T,\varepsilon)$ is the Ginzburg–Landau parameter given by[91]:

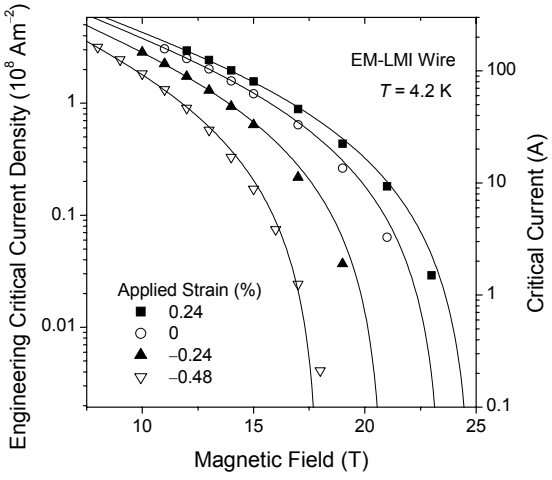

Figure 3.4. Engineering critical current density (and critical current) of the EM-LMI wire as a function of magnetic field at 4.2 K and at different applied strains between 0.24% and –0.48%. The symbols show the measured data, and the lines the Interpolative Scaling Law.

$$\kappa_1^*(T,\varepsilon)=\frac{1.03\left[\eta(\varepsilon)\right]^{1/2}B_{C2}^*(T,\varepsilon)}{\mu_0^{1/2}\left[\gamma(\varepsilon)\right]^{1/2}T_C^*(\varepsilon)\left(1-t^2\right)}, \tag{1.4}$$

where $\eta(\varepsilon)=1-12.2\left(k_B T_C/\hbar\omega_{ln}\right)^2\ln\left(\hbar\omega_{ln}/3k_B T_C\right)$ is a strong-coupling correction to the BCS value of the ratio $\mu_0\gamma T_C^2/\left[B_C(0)\right]^2$ (ω_{ln} is an average phonon frequency) and $\gamma(\varepsilon)$ is the electronic specific heat coefficient[91,96,102]. Combining Equations (1.2) and (1.4), and incorporating $A'(\varepsilon)$, $\eta(\varepsilon)$, and $\gamma(\varepsilon)$ into a single strain-dependent parameter $A(\varepsilon)$ results in the following expression for $J_C(B,T,\varepsilon)$:

$$J_C(B,T,\varepsilon)=A(\varepsilon)\left[T_C^*(\varepsilon)\left(1-t^2\right)\right]^m\left[B_{C2}^*(T,\varepsilon)\right]^{n-m-1}b^{p-1}(1-b)^q. \tag{1.5}$$

The scaling law therefore involves the exponents *m*, *n*, *p*, *q*, and *v*, and the parameters $A(\varepsilon)$, $T_C^*(\varepsilon)$, and $B_{C2}^*(0,\varepsilon)$. These strain-dependent parameters are constrained to be fourth-order polynomial functions of applied strain with a stationary point (e.g. maximum) at a common value, ε_M. Similarly to previous work, the exponent

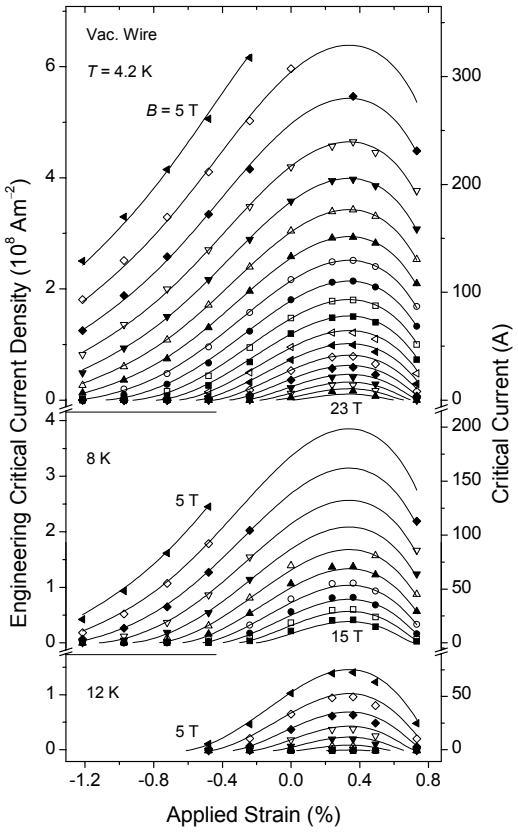

Figure 3.5. Engineering critical current density (and critical current) of the Vac wire as a function of applied strain at integer magnetic fields between 5 and 23 T and at 4.2, 8, and 12 K. The symbols show the measured data and the solid lines the Interpolative Scaling Law.

m is set to 2, implying the relation $J_C \propto 1/\left(\kappa_1^*\right)^2$ [28,79]. The Interpolative Scaling Law enables extremely accurate parameterisations of the J_C data over the large ranges of magnetic field, temperature, and strain that were investigated, with RMS differences between the measured and calculated values of 1.40 A for the EM-LMI wire and 2.05 A for the Vac wire. The parameterisations are compared graphically with the measured $J_C\left(B,T,\varepsilon\right)$ in Figures 3.3–3.5.

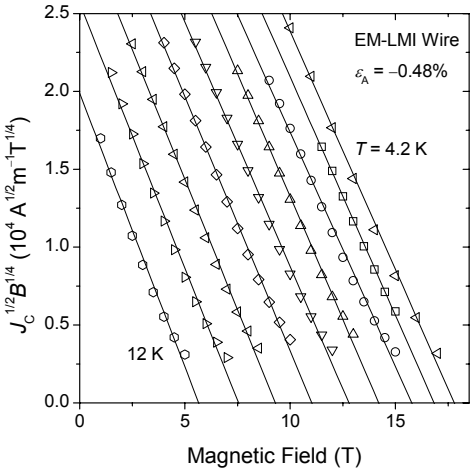

Figure 3.6. Kramer plots for the EM-LMI wire at –0.48% applied strain and at 4.2 K and 1 K increments between 5 and 10 K. The symbols show the measured data, and the lines the best straight-line fits.

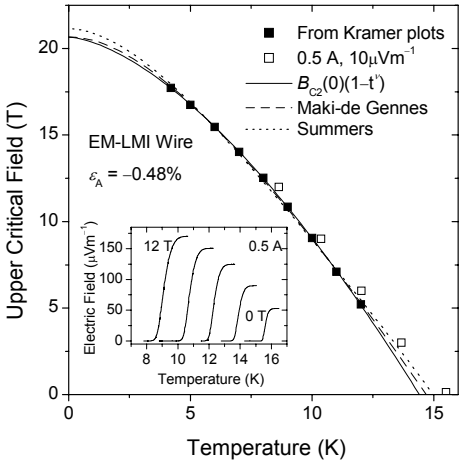

Figure 3.7. Upper critical field as a function of temperature for the EM-LMI wire at –0.48% applied strain (i.e. close to the operating strain of the TFMC[4]). The closed symbols show B_{C2}^* obtained from Kramer plots (see Figure 3.6) and the lines show various fits to these data. The open symbols show the values of B_{C2}^ρ determined at 0.5 A and 10 μVm^{-1} from the E–T data shown in the inset.

For the EM-LMI wire, the optimum values of p (0.474) and q (1.95) are close to the commonly-used "Kramer values" ($p = 1/2$ and $q = 2$)[64,79,101]. Figure 3.6 shows Kramer plots ($J_C^{1/2}B^{1/4}$ versus B) for the EM-LMI wire at –0.48% applied strain: the good straight-line fits also demonstrate that the magnetic field dependence of J_C can be parameterised with $p = 1/2$ and $q = 2$ (at least for $I_C > 1$ A). For the Vac wire, however, the optimum values of p (0.468) and q (1.48) are further from the Kramer values, and setting $p = 1/2$ and $q = 2$ results in a ~25% increase in the RMS error for the best fit (from 2.05 A to

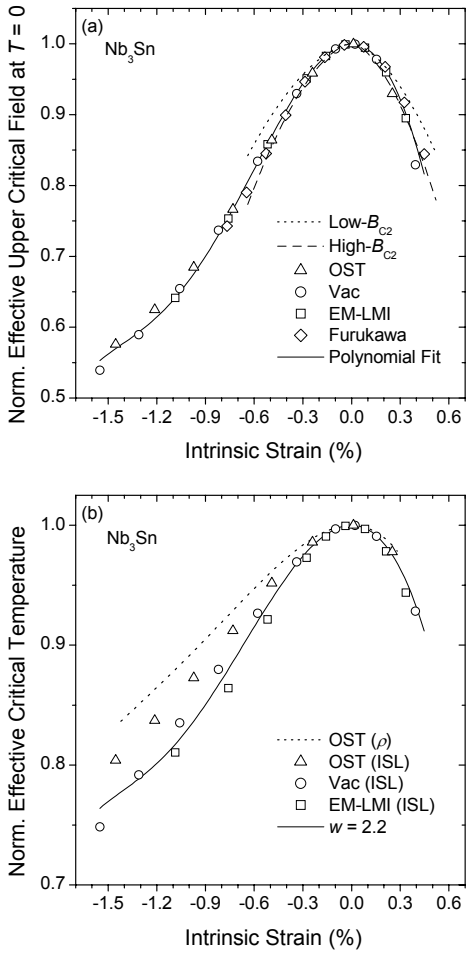

Figure 3.8. (a) The normalised effective upper critical field at $T = 0$ and (b) normalised effective critical temperature as a function of intrinsic strain for different Nb_3Sn wires. In (a), the symbols show data for wires measured in Durham and the solid line shows a universal fit to these data, while the dotted line is for previous measurements on low-$B_{C2}^*(0)$ wires[1] and the dashed line for high-$B_{C2}^*(0)$ wires[2]. For the Furukawa data and the dashed and dotted lines, $B_{C2}^*(0)$ was calculated from the $B_{C2}^*(4.2\text{ K})$ data using Equations (1.3) and (1.9). In (b), the solid line is calculated using the universal fit to the normalised $B_{C2}^*(0)$ data and the power-law relation with $w = 2.2$, while the dotted line shows $T_C^\rho(\varepsilon_I)$ data obtained from resistivity measurements for the OST wire.

2.60 A) and unphysically high values for the effective upper critical field, with $B^*_{C2}(0, \varepsilon_I = 0) \approx 35$ T.

Figure 3.7 shows the upper critical field as a function of temperature for the EM-LMI wire at –0.48% applied strain. It can be seen that Equation (1.3) provides a good fit to the $B^*_{C2}(T, \varepsilon)$ data obtained from the Kramer plots in Figure 3.6 (with $\nu \approx 1.5$ in this case). Two other fits to these data are also shown: the Maki-de Gennes relation for a dirty superconductor with no Pauli paramagnetic limiting[92,103,104], which fits the data well, and the Summers Scaling Law relation [Equation (4.7)], which is somewhat less accurate. Also shown in Figure 3.7 are the values of upper critical field [$B^{\rho}_{C2}(T, \varepsilon)$] determined from the *E*–*T* characteristics for a current of 0.5 A and an electric-field criterion of 10 μVm^{-1} (5–20% of the transition height). Note that the equivalence between *E*–*T* and *E*–*J* data means that these values of $B^{\rho}_{C2}(T, \varepsilon)$ are also the values of *B* where J_C at 10 μVm^{-1} is 0.5 A. These low-current-density values are ~0.4 K higher for $B \geq 4$ T and ~0.8 K higher for $B = 0$ than the values obtained from the Kramer plots [and Equation (1.3)]. At this value of strain, the measured J_C goes to zero less rapidly than the Kramer lines, with a "tail" that is usually associated with the distribution of T_C and B_{C2} in technological wires[68,91]. Determining T_C from measurements at very low current densities ($B \approx 0$) provides a method for assessing the strain-state of the model coils at cryogenic temperatures, although it must be noted that the measured value of $T^{\rho}_C(B = 0) = 15.5$ K at –0.76% intrinsic strain differs quite considerably from the scaling-law parameter T^*_C (= 14.6 K). Self-field effects may also be important in such measurements.

Figure 3.8(a) shows normalised values of $B^*_{C2}(0, \varepsilon_I)$ for the EM-LMI and Vac wires, as well as additional data for the Furukawa wire[11] and an OST wire[91]. It can be seen that $B^*_{C2}(0, \varepsilon_I)$ for these Nb_3Sn wires follows an approximately universal relation, which is also largely independent of the choice of *p* and *q*[1]. Hence the higher strain-sensitivity of J_C for the EM-LMI wire in relation to the other wires (see Figure 3.2) is due to lower absolute values of $B^*_{C2}(0)$ and T^*_C at zero intrinsic strain. Figure 3.8(a) also includes two different datasets obtained from the literature, represented by best-fit lines[1,2]. These values were calculated from the $B^*_{C2}(4.2\text{ K}, \varepsilon_I)$ data using Equations (1.3) and (4.9), although the differences between the normalised values of B^*_{C2} at $T = 0$ and 4.2 K are not large (the Furukawa values were also calculated in this way)[85]. The less strain-sensitive line taken from Ekin's well-known work represents relatively clean Nb_3Sn with low values of $B^*_{C2}(0, \varepsilon_I = 0)$ of ~24 T[1], while the more strain-sensitive line is for Nb_3Sn wires with Ta additions and higher values of $B^*_{C2}(0, \varepsilon_I = 0)$[2]. The ITER-candidate wires and other recently-developed Nb_3Sn wires have ternary additions of Ti (EM-LMI) or Ta (Vac) and relatively high values of $B^*_{C2}(0, \varepsilon_I = 0)$: typically 28–30 T. Hence the better agreement with the previous ternary data rather than the binary data correlates with the higher values of $B^*_{C2}(0, \varepsilon_I = 0)$. The differences between binary and ternary Nb_3Sn are also predicted by microscopic theory (see Section 3.4), but have been somewhat neglected in the past[85].

Figure 3.8(b) shows normalised values of $T_C^*(\varepsilon_I)$ for the EM-LMI, Vac, and OST wires: it can be seen that there is more variation between the different wires, although for the two ITER-candidate wires the differences are only ~4%. Also shown in Figure 3.8(b) are $T_C^\rho(\varepsilon_I)$ data obtained from resistivity measurements for the OST wire, which can be seen to be less strain-sensitive than the scaling-law values. This behaviour is observed for the $B_{C2}^\rho(T,\varepsilon)$ and $T_C^\rho(\varepsilon_I)$ data for all of the wires we have investigated, and can be related to strain (and temperature) variations in the low-current-density tails discussed above. A reasonable interpretation of the difference is that the scaling law values of B_{C2}^* (and T_C^*) are characteristic values for the bulk of the material, while the resistivity values give the maxima of the distributions in B_{C2} (and T_C)[1,91,105].

3.3.2 Comparison with Summers Scaling Law

The Summers Scaling Law for $J_C(B,T,\varepsilon)$ involves the following relations[1,85,86]:

$$J_C(B,T,\varepsilon) = C(\varepsilon)\left(1-t^2\right)^2\left[B_{C2}^*(0,\varepsilon)\right]^{-1/2} b^{-1/2}(1-b)^2 \tag{1.6}$$

$$B_{C2}^*(T,\varepsilon) = B_{C2}^*(0,\varepsilon)\left(1-t^2\right)\left[1-0.31t^2(1-1.77\ln t)\right] \tag{1.7}$$

$$\frac{B_{C2}^*(0,\varepsilon_I)}{B_{C2}^*(0,0)} = \left[\frac{T_C^*(\varepsilon_I)}{T_C^*(0)}\right]^3 = \left[\frac{C(\varepsilon_I)}{C(0)}\right]^2 = 1-a\left|\varepsilon_I\right|^{1.7}, \tag{1.8}$$

with $a = 1250$ for $\varepsilon_I > 0$ and $a = 900$ for $\varepsilon_I < 0$. The scaling law is commonly used for ITER-candidate conductors[4,5,9,86], but we have found that it predicts a weaker strain-dependence for J_C than is observed and hence cannot parameterise ternary Nb_3Sn data accurately—typical RMS differences are ~10 A. Figure 3.3 explicitly shows a comparison between the measured data for the EM-LMI wire and the values for $J_C(12\text{ T},4.2\text{ K},\varepsilon_I)$ calculated using the Summers Scaling Law with the free parameters obtained by fitting the data for $|\varepsilon_I| < 0.22\%$; similar disagreement is also observed for the Vac wire[4,5].

We can improve the accuracy of the Summers fits over a limited strain range ($\varepsilon_I \geq -0.8\%$) by leaving a as a free parameter: for the EM-LMI wire, the best-fit is obtained with $a = 1840$ ($\varepsilon_I > 0$) and 1160 ($\varepsilon_I < 0$) and has an RMS error of 2.4 A, while for the Vac wire, values of $a = 1900$ and 1160, and an RMS error of 2.4 A are obtained. These values of a are comparable with previous values for high-$B_{C2}^*(0)$ Nb_3Sn [$a = 1690$ for $\varepsilon_I > 0$ and 1210 for $\varepsilon_I < 0$, see Figure 3.8(a)][2]. However, Figure 3.8(a) shows that, even for optimum values of a, Equation (1.8) begins to deviate significantly from the measured $B_{C2}(0,\varepsilon_I)$ at a compressive strain of $\varepsilon_I \approx -0.7\%$ (close to the strain at which the TFMC operates). Note, however, that Equation (1.8) is based upon measurements that were only performed at tensile applied strains corresponding to $\varepsilon_I \geq -0.5\%$[1]. The data in this section have second-derivatives (with respect to ε_I) of both $B_{C2}(0,\varepsilon_I)$ [Figure 3.8(a)] and $J_C(12\text{ T},4.2\text{ K},\varepsilon_I)$ (Figures 3.3 and 3.5) that change sign at

$\varepsilon_I \approx -0.7\%$: behaviour which cannot be reproduced by Equation (1.8). Hence we will set aside this function for the strain-dependence as polynomial functions seem preferable—especially if large strain ranges are being investigated.

3.4 Relationship between strain-dependent superconducting parameters

In this section, we will consider the relationship between $B_{C2}(0,\varepsilon_I)$ and $T_C(\varepsilon_I)$, presenting our experimental data for a number of wires and analysing the relationship using microscopic theory. For the analysis we adopt a similar approach to Welch[71], using Eliashberg theory (the Allen and Dynes equation[94,95]) and Ginzburg–Landau–Abrikosov–Gor'kov theory[92,96,97] to provide a better understanding of the empirical scaling-law relations, and the microscopic mechanisms responsible for the strain effects in *A*15 (Nb_3Sn and Nb_3Al) superconducting wires.

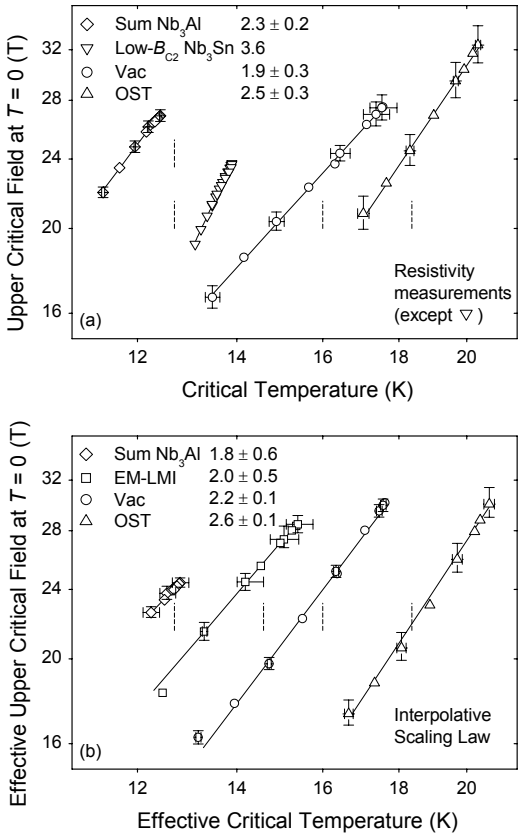

Figure 3.9. A log–log plot of upper critical field at $T = 0$ versus critical temperature for different *A*15 wires: (a) data from resistivity and other measurements; (b) effective values obtained by fitting the J_C data using the Interpolative Scaling Law. The solid lines show the best power-law fits and the legend shows the values of the exponent *w*. Except for the Vac wire, the data have been shifted horizontally for clarity (the vertical dashed lines show $T_C = 16$ K for each wire).

3.4.1 Power-law relationship and experimental data

A power-law relationship between $B_{C2}(0,\varepsilon_I)$ and $T_C(\varepsilon_I)$ was first proposed by Ekin (although originally in terms of the upper critical field at 4.2 K)[1]:

$$\frac{B_{C2}(0,\varepsilon_I)}{B_{C2}(0,\varepsilon_I=0)}=\left(\frac{T_C(\varepsilon_I)}{T_C(\varepsilon_I=0)}\right)^w. \tag{1.9}$$

The exponent $w \approx 3$ was estimated using $B^*_{C2}(4.2\text{ K},\varepsilon_I)$ data obtained from J_C measurements on binary Nb_3Sn wires[1] and $T_C^\chi(\varepsilon_I)$ data from susceptibility measurements on a different set of binary Nb_3Sn wires[20]. The power-law with $w=3$ is currently used in a number of scaling laws for $J_C(B,T,\varepsilon)$ [14,85]. The original (low-B^*_{C2}) data are shown on a log–log plot in Figure 3.9(a), with $B^*_{C2}(0,\varepsilon_I)$ calculated from the $B^*_{C2}(4.2\text{ K},\varepsilon_I)$ and $T_C^\chi(\varepsilon_I)$ data using the Maki-de Gennes relation: the best fit gives $w=3.6$ (the value is 3.8 if the upper critical field data at 4.2 K are used directly). However, assuming that $T_C^\chi(\varepsilon_I)$ and $T_C^\rho(\varepsilon_I)$ behave similarly, the different strain-dependences observed for our scaling-law and resistivity data imply that artificially high values of w may be obtained from combining B^*_{C2} and T_C^χ data. Also shown in Figure 3.9(a) are values obtained from low-current-density measurements of $B^\rho_{C2}(T,\varepsilon_I)$ for the Vac Nb_3Sn wire ($I=0.5$ A), the OST Nb_3Sn wire (30 mA)[91], and a Sumitomo Nb_3Al wire (30 mA)[28], where Equation (1.3) was used to extrapolate to $T=0$ and T_C. It can be seen that for these $A15$ wires, the values of w are all between ~1.9 and ~2.5. In addition, Figure 3.9(b) shows the values of $B^*_{C2}(0,\varepsilon_I)$ and $T^*_C(\varepsilon_I)$ obtained using the Interpolative Scaling Law from the comprehensive $J_C(B,T,\varepsilon)$ datasets available for four different $A15$ wires. These are also consistent with the power law and give similar values of w. For Nb_3Sn wires characterised by high values of $B^*_{C2}(0,\varepsilon_I=0)$ (approximately 28–30 T), the values of $w \le 2.5$ are therefore similar for both resistivity and scaling-law data, despite the different strain-dependences observed, and are significantly lower than the values ($w \ge 3$) obtained for binary, low-B^*_{C2} (~24 T) Nb_3Sn wires.

Table 3.1. Microscopic parameters determined from tunnelling measurements on Nb_3Sn[106] and Nb_3Al (23 at. % Al)[107]. Also shown are the values of T_C calculated using Equation (4.10), and the values of μ^* required for Equation (4.10) to give the measured values of T_C (shown in brackets).

	Nb_3Sn	Nb_3Al
ω_{ln} (meV)	10.8	9.5
ω_2 (meV)	15.0	13.5
λ	1.8 ± 0.15	1.7 ± 0.05
μ^*	0.16 ± 0.03 (0.14)	0.15 ± 0.02 (0.10)
T_C (K) calc. (meas.)	16.2 (17.5)	13.9 (16.4)

3.4.2 Analysis using microscopic theory

The Allen and Dynes equation gives the critical temperature of strongly-coupled superconductors in terms of various microscopic parameters[94,95]:

$$k_B T_C = \frac{f_1 f_2 \hbar \omega_{ln}}{1.20} \exp\left(-\frac{1.04(1+\lambda)}{\lambda - \mu^* - 0.62\lambda\mu^*} \right), \tag{1.10}$$

where ω_{ln} is a weighted logarithmically-averaged phonon frequency, λ is the electron-phonon coupling parameter, μ^* is the effective Coulomb-repulsion parameter, and f_1 and f_2 are correction factors of order unity[94]. The electron-phonon coupling parameter is related to the bare electronic density of states at the Fermi energy $N(0)$ and a weighted RMS phonon frequency ω_2 by[95]:

$$\lambda = \frac{N(0)\langle I^2 \rangle}{M\omega_2^2}, \tag{1.11}$$

where $\langle I^2 \rangle$ is the average over the Fermi surface of the electron-phonon matrix element squared and M is the average ionic mass. The electronic specific heat coefficient γ is related to $N(0)$ and λ by[95]:

$$\gamma = \tfrac{2}{3}\pi^2 k_B^2 N(0)(1+\lambda). \tag{1.12}$$

The parameters ω_{ln}, ω_2, λ, and μ^* determined from tunnelling measurements on

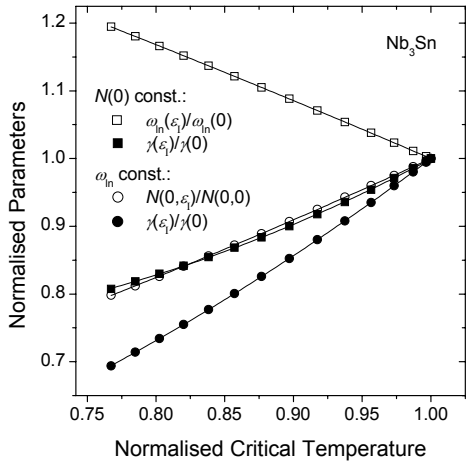

Figure 3.10. Calculated microscopic parameters for Nb_3Sn as a function of critical temperature, with all quantities normalised to their values at zero intrinsic strain. Square symbols: ω_{ln} and γ calculated assuming constant $N(0)$; round symbols: $N(0)$ and γ calculated assuming constant ω_{ln}. The maximum reduction in critical temperature (23%) corresponds to the measured reduction for the Vac wire at −1.55% intrinsic strain.

Nb_3Sn[106] and off-stoichiometric Nb_3Al[107] are shown in Table 3.1. In the analysis described below, we will use μ^* as a free parameter to fit the measured zero-intrinsic-strain values of T_C, which can generally be achieved with relatively small changes in μ^* (see Table 3.1)[96]. We will make the assumption that the variations of μ^* or $\langle I^2 \rangle$ with strain are considerably less important than the other parameters, and hence they can be considered as constants. We will also assume that the strain-dependence of the normalised average phonon frequencies (ω_{ln} and ω_2) is the same[90].

The variation of T_C with uniaxial strain can be related to variations in the average phonon frequencies and/or variations in the bare electronic density of states at the Fermi energy. Due to a lack of detailed information in the literature about the uniaxial strain-dependence of these parameters, we will begin by considering the two extreme cases: firstly that the strain-dependence of T_C is entirely due to the strain-dependence of the average phonon frequencies, and secondly that strain only affects electronic properties [i.e. $N(0)$]. For Nb_3Sn, Figure 3.10 shows how the various parameters depend on T_C in these two cases: in the first case, ω_{ln} increases approximately linearly with decreasing T_C and, in the second case, $N(0)$ decreases approximately linearly with decreasing T_C. In both cases, the magnitude of the change is ~20% for a decrease in T_C of 23%, corresponding to $\varepsilon_I = -1.55\%$ for the Vac wire. The data shown in Figure 3.10 are calculated for Nb_3Sn with $T_C(\varepsilon_I = 0) = 17.5\,\mathrm{K}$ (Vac wire), but the relationships between the reduced parameters and the reduced critical temperature are insensitive (to within ~1%) to quite large variations in $T_C(\varepsilon_I = 0)$ (~1 K). These relationships are also similar (to within ~1%) for Nb_3Al, although the critical temperature of Nb_3Al is a factor of ~3 less sensitive to uniaxial strain[28].

The upper critical field at $T = 0$ can be calculated using the following expression[92,96,97]:

$$B_{C2}(0) = 0.973\,\mu_0^{1/2}\eta_{B_{C2}(0)}\kappa^*(0,\lambda_{tr})\left[R(\lambda_{tr})\right]^{-1} \times\left[7.30\times10^{37}\left(\gamma T_C/S\right)^2 + 2.78\times10^6\,\gamma T_C\rho_n\right], \tag{1.13}$$

where $\eta_{B_{C2}(0)}$ is a strong-coupling correction of order unity[96], κ^* is the reduced temperature-dependent Ginzburg–Landau parameter [$\kappa^*(0,0) = 1.26$ and $\kappa^*(0,\infty) = 1.20$], $R(\lambda_{tr})(1+\lambda_{tr})^{-1}$ is the Gor'kov function [$R(0) = 1$ and $R(\infty) = 1.17$], λ_{tr} is the reduced mean collision frequency given by[97]:

$$\lambda_{tr} = 0.882\,\xi_0^*/l_{tr} = 3.81\times10^{-32}\,S^2\rho_n/(\gamma T_C), \tag{1.14}$$

ξ_0^* is the renormalised BCS coherence length, l_{tr} is the electron mean free path, S is the Fermi surface area, and ρ_n is the low-temperature normal-state resistivity.

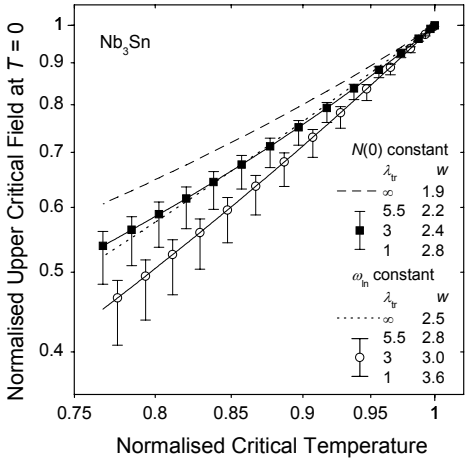

Figure 3.11. Log–log plot of the calculated upper critical field at $T = 0$ versus critical temperature for Nb_3Sn, with both quantities normalised to their values at zero intrinsic strain. Two cases are considered: (a) $N(0)$ is constant, and ω_{ln} and ω_2 vary with uniaxial strain, and (b) ω_{ln} and ω_2 are constant, and $N(0)$ varies with strain. The symbols are for $\lambda_{tr}(\varepsilon_I = 0) = 3$, the error bars for $\lambda_{tr}(\varepsilon_I = 0) = 5.5$ and 1 at their extrema, and the dotted and dashed lines for $\lambda_{tr}(\varepsilon_I = 0) = \infty$ (extreme dirty limit). The maximum reduction in critical temperature (23%) corresponds to the measured reduction for the Vac wire at −1.55% intrinsic strain.

Both S and ρ_n are expected to be largely independent of uniaxial strain, and are considered as constants with $S = (1.7 \pm 0.7) \times 10^{21}$ m^2 for Nb_3Sn[97] and $(1.8 \pm 0.7) \times 10^{21}$ m^2 for Nb_3Al[108]. For $\lambda_{tr} \ll 1$ (the "clean limit"), the first term in the square brackets in Equation (1.13) dominates and $B_{C2}(0) \propto (\gamma T_C)^2$ whereas for $\lambda_{tr} \gg 1$ (the "dirty limit"), the second term dominates and $B_{C2}(0) \propto \gamma T_C$. For intermediate values of λ_{tr}, $B_{C2}(0)$ is approximately proportional to $(\gamma T_C)^v$, where the exponent v depends only on λ_{tr} and has a value between ~1 and ~2. Analysis of data for monofilamentary bronze-route Nb_3Sn wires[109] shows that $\lambda_{tr}(\varepsilon_I \approx 0) = 3 \pm 2.5$ for materials with tertiary additions (Ti, Ta) and optimal upper critical fields, which are similar to the technological wires that we have measured (the uncertainty in λ_{tr} given here is calculated from the uncertainty in S). By setting $\lambda_{tr}(\varepsilon_I = 0) = 3$, the variation of $B_{C2}(0)$ can be calculated using Equations (1.13) and (1.14), with $\gamma(\varepsilon_I = 0)$ and ρ_n calculated from the measured value of $B_{C2}(0)$ at zero intrinsic strain [for the Vac wire with $B_{C2}(0, \varepsilon_I = 0) = 27.6$ T, we get values consistent with the literature[97], $\rho_n = 41$ μΩcm and $\gamma(\varepsilon_I = 0) = 860$ Jm^{-3}K^{-2}, although the conclusions given below are independent of the value of $B_{C2}(0,0)$].

Figure 3.11 shows a normalised log–log plot of the calculated values of $B_{C2}(0, \varepsilon_I)$ as a function of $T_C(\varepsilon_I)$ for Nb_3Sn. It can be seen that the relationship between $B_{C2}(0)$

and T_C is quite accurately described by a power law [Equation (1.9)] with, for $\lambda_{tr}(\varepsilon_I = 0) = 3$, the exponent $w = 2.4$ for the case where only ω_{ln} varies with uniaxial strain, and $w = 3.0$ for the case where only $N(0)$ varies with strain. These values are for fits over the range $0.77 \le T_C(\varepsilon_I)/T_C(0) \le 1$, which is relevant for comparison with our experimental data in Figure 3.9 although w can vary depending on the exact temperature range chosen by about ±0.1. The deviations from the power law are such that w is larger (by ≤ 0.6) closer to $T_C(\varepsilon_I)/T_C(0) = 1$. We have investigated alternative functional forms that describe the theoretical data in Figure 3.11 rather better, but have not used them in this section because the power law is reasonably accurate for both clean and dirty superconductors and the improvement in J_C parameterisation was not sufficiently large. Given the large uncertainties in λ_{tr}, we have also shown in Figure 3.11 the results and values of w for $\lambda_{tr}(\varepsilon_I = 0) = 5.5$ and 1 [1 is considered as the lower bound for Nb_3Sn with $B_{C2}(0, \varepsilon_I = 0) \ge 27$ T], as well as for the extreme dirty limit ($\lambda_{tr} = \infty$). It can be seen that w increases as $\lambda_{tr}(\varepsilon_I = 0)$ decreases or the relative contribution of variations in $N(0)$ increases. Measurements on Nb_3Al thin films[108] imply that $\lambda_{tr} \approx 7$, corresponding to $w \approx 2.5$ (variations only in ω_{ln}) and $w \approx 2.9$ [variations only in $N(0)$] for the range $T_C(\varepsilon_I)/T_C(0) \ge 0.92$ ($\varepsilon_I = -1.4\%$ for the Nb_3Al Sumitomo wire).

3.4.3 Comparison of theoretical and experimental results

Comparing the theoretical values for w (Figure 3.11) with the experimental data (Figure 3.9), it can be seen that the agreement is considerably better if the strain-dependence of the average phonon frequencies is the dominant factor. Assuming $\lambda_{tr}(\varepsilon_I = 0) = 3$, microscopic theory gives $w = 2.4$ if $N(0)$ is constant and higher values if $N(0)$ varies, compared to the typical experimental values for high-$B^*_{C2}(0)$ wires between ~2 and ~2.5. Our results are therefore in agreement with the implications of Testardi's work[110-112], who related the strain-dependence of T_C to the large phonon anharmonicity effects in $A15$ superconductors[113,114]. Alternatively, various properties of $A15$ compounds have been related to peaks in the electronic density of states near the Fermi energy[115,116]. However, it has been noted that tertiary additions would broaden these peaks and therefore cause a reduction in the strain-sensitivity of T_C if the variations in $N(0)$ were indeed the dominant factor, whereas the opposite effect is observed experimentally [see Figure 3.8(a)][2]. Band-structure calculations[117-119] also show that there is only a relatively small decrease in $N(0)$ (< 3%) for the transition from the cubic to the tetragonal phases of Nb_3Sn. Here, the distortion of the unit cell in the tetragonal phase[112] can be considered as equivalent to a macroscopic strain of $\varepsilon_I \approx -0.44\%$ (calculated by equating the deviatoric strain components[70]): the lower values of T_C (~1 K in otherwise equivalent materials)[120] and $B_{C2}(0)$ (~3 T)[121] observed for the tetragonal phase are indeed broadly consistent with our strain results (see Figure 3.8).

Some other results in the literature can be used to assess the validity of the assumptions made in the analysis and the conclusions about the microscopic mechanism. Due to a lack of information about uniaxial strain effects, it is necessary to discuss

measurements of microscopic properties as a function of various other adjustable parameters. In measurements on Nb_3Sn under hydrostatic pressure[90], changes in both $N(0)$ and ω_{ln} were observed, and the parameter $\langle I^2 \rangle$ increased slightly as $N(0)$ decreased (in contrast to our assumption of $\langle I^2 \rangle = \text{constant}$). The large differences between the effect of non-hydrostatic (uniaxial) strains and hydrostatic strains on the superconducting properties (T_C)[71] may indicate that there is a different mechanism operating in each case (indeed, the dependences are of opposite sign in V_3Si[2,122]). Nevertheless, such a correlation between $N(0)$ and $\langle I^2 \rangle$[123] would tend to increase the calculated value of w and therefore, from the comparison with the experimental data, further strengthen the case for phononic changes being the dominant factor. We also note that experimental[124] and computational[125] data show that $\langle I^2 \rangle$ is approximately constant for series of different niobium-based superconductors. Tunnelling measurements[126] on Nb-Sn samples with varying stoichiometry show that μ^* is approximately constant for variations in T_C of ~7 K, consistent with our assumption for the case of uniaxial strain. In these measurements, the largest changes in $\alpha^2 F(\omega)$ occurred at lower frequencies and therefore ω_{ln} varied more than ω_2 (by ~50% for variations in T_C of ~3 K): this effect would also tend to increase the calculated value of w (and further emphasise the role of phononic changes).

Comparison between our experimental data and theory provides strong evidence that in high-B_{C2}^* Nb_3Sn, uniaxial strain predominantly changes the average phonon frequencies rather than the electronic density of states at the Fermi energy. The theory—in which w decreases with increasing impurity scattering rate—also provides a straightforward explanation for low values of w (≤ 2.5) for ternary Nb_3Sn compared to the binary materials (~3.6)[1,20]. Estimating $\lambda_{tr} \approx 1$ for the binary Nb_3Sn wires[109], and considering values of $T_C(\varepsilon_I)/T_C(0) \geq 0.94$, gives $w \approx 3.3$ for the case where phononic changes dominate and $w \approx 3.9$ for the case where the electronic changes dominate.

Table 3.2. RMS errors for fits to the comprehensive $J_C(B,T,\varepsilon)$ data using various scaling laws.

Scaling Law	RMS error (mean I_c) (A)		
	EM-LMI	Vac	OST
	(42.5)	(61.4)	(35.7)
ISL	1.40	2.05	1.35
Simplified ISL (u free)	1.40	2.50	1.75
Simplified ISL (u = 0)	1.40	2.50	1.80
Simplified ISL (u = 1.25)	1.55	3.20	1.85
Simplified ISL [free: $A(0)$, $T_C^*(0)$, $B_{C2}^*(0,0)$, ε_M]	2.10	6.60	5.70

Table 3.3. Simplified Interpolative Scaling Law parameters for (a) the EM-LMI wire, (b) the Vac wire, and (c) the OST wire. Note that for the values given in the table intrinsic strain is in units of percent and the calculated J_C is the engineering critical current density in units of Am^{-2}.

(a) EM-LMI Wire

P	q	n	ν	w	u	ε_M (%)
0.4741	1.953	2.338	1.446	1.936	–0.056	0.2786

$A(0)$ ($Am^{-2}T^{3-n}K^{-2}$)	$T_C^*(0)$ (K)	$B_{C2}^*(0,0)$ (T)	c_2	c_3	c_4
2.446×10^7	16.89	28.54	−0.7697	−0.4913	−0.0538

(b) Vac Wire

P	q	n	ν	w	u	ε_M (%)
0.4625	1.452	2.457	1.225	2.216	0.051	0.3404

$A(0)$ ($Am^{-2}T^{3-n}K^{-2}$)	$T_C^*(0)$ (K)	$B_{C2}^*(0,0)$ (T)	c_2	c_3	c_4
9.460×10^6	17.58	29.59	−0.6602	−0.4656	−0.1075

(c) OST Wire

p	q	n	ν	w	u	ε_M (%)
0.4763	2.150	3.069	1.240	2.545	–0.912	0.2421

$A(0)$ ($Am^{-2}T^{3-n}K^{-2}$)	$T_C^*(0)$ (K)	$B_{C2}^*(0,0)$ (T)	c_2	c_3	c_4
6.417×10^6	18.00	29.17	–0.6457	–0.4514	–0.1009

3.5 Simplified interpolative scaling law for $J_C(B,T,\varepsilon)$

In this section, a simplified version of the Interpolative Scaling Law involving fewer free parameters is presented, and the typical accuracy that can be expected when using this scaling law to extrapolate from partial $J_C(B,T,\varepsilon)$ datasets is quantified[1,85].

3.5.1 Parameterisations of complete $J_C(B,T,\varepsilon)$ datasets

Firstly, we assume that the power-law relation between $B_{C2}(0,\varepsilon_I)$ and $T_C(\varepsilon_I)$ given by Equation (1.9) is valid, which was shown to be the case for the experimental and theoretical results presented in Section 3.4. Secondly, we note that the optimum polynomial functions for $A(\varepsilon_I)$ are generally quite complex (>1 turning point), but have

large associated uncertainties (for example, are sensitive to the fitting procedure) and vary considerably between different wires. Hence for simplicity (and without much loss of accuracy, as shown below), it will be assumed that $A(\varepsilon_I)$ can also be constrained as a power-law function of $T_C(\varepsilon_I)$[85]. The simplified Interpolative Scaling Law therefore involves the following relations (the exponent *m* has been set to 2):

$$J_C(B,T,\varepsilon_I) = A(\varepsilon_I)\left[T_C^*(\varepsilon_I)\left(1-t^2\right)\right]^2\left[B_{C2}^*(T,\varepsilon_I)\right]^{n-3} b^{p-1}(1-b)^q \tag{1.15}$$

$$B_{C2}^*(T,\varepsilon_I) = B_{C2}^*(0,\varepsilon_I)\left(1-t^v\right) \tag{1.16}$$

$$\left(\frac{A(\varepsilon_I)}{A(0)}\right)^{1/u} = \left(\frac{B_{C2}^*(0,\varepsilon_I)}{B_{C2}^*(0,0)}\right)^{1/w} = \frac{T_C^*(\varepsilon_I)}{T_C^*(0)} \tag{1.17}$$

$$\frac{B_{C2}^*(0,\varepsilon_I)}{B_{C2}^*(0,0)} = 1 + c_2\varepsilon_I^2 + c_3\varepsilon_I^3 + c_4\varepsilon_I^4, \tag{1.18}$$

which we take to be valid for different electron-phonon coupling strengths and impurity scattering rates. Using this simplified scaling law to fit the complete $J_C(B,T,\varepsilon)$ datasets for the Vac, EM-LMI and OST[91] Nb_3Sn wires gives RMS errors of ~1.5–2.5 A, as shown in Table 3.2. The simplified Interpolative Scaling Law involves 13 free parameters (compared to 17 for the ISL), the optimum values of which are shown in Table 3.3. Table 3.2 also shows errors for the simplified ISL with fixed values for *u* [the power-law exponent for $A(\varepsilon_I)$, discussed below] and with the set of universal values proposed in the next section for the parameterisations of partial datasets [in this case, there are 4 free parameters: $A(0)$, $B_{C2}^*(0,0)$, $T_C^*(0)$, and ε_M].

Using Equations (1.2), (1.4), and (1.5), the prefactor $A(\varepsilon_I)$ can be written as:

$$A(\varepsilon_I) = 0.97\mu_0^{1/2}A'(\varepsilon_I)\gamma(\varepsilon_I)/\eta(\varepsilon_I). \tag{1.19}$$

The results from microscopic theory presented in Section 3.4.2 allow the term $\gamma(\varepsilon_I)/\eta(\varepsilon_I)$ in Equation (1.19) to be related to $T_C^*(\varepsilon_I)$. Assuming that $A'(\varepsilon_I) = \text{constant}$, an approximate power-law relationship between $A(\varepsilon_I)$ and $T_C^*(\varepsilon_I)$ is then obtained with exponent $u = 1.25$ (variations only in ω_{ln}) or $u = 1.65$ [variations only in $N(0)$]. As shown in Table 3.2, however, the fits to the complete datasets using the simplified Interpolative Scaling Law with $u = 1.25$ have RMS errors that are ~30% higher than the fits with *u* as a free parameter. The optimum values for *u* are approximately zero for the EM-LMI and Vac wires and approximately −1 for the OST wire, although the latter value has a large associated uncertainty, as shown by the small increase in the error that is observed when *u* is fixed at zero (see Table 3.2). Hence the large uncertainties (and our assumption about the value of the exponent *m*) prevent any definite physical interpretation of $A'(\varepsilon_I)$ at this stage[23,101].

The optimum values of u in the simplified Interpolative Scaling Law can also be compared with the Summers Scaling Law, in which the variation of the prefactor was fixed so that $F_{\mathrm{PM}}\left(0,\varepsilon_{\mathrm{I}}\right) \propto \left[B^{*}_{\mathrm{C2}}\left(0,\varepsilon_{\mathrm{I}}\right)\right]^{n'}$ with $n' = 1$, in approximate agreement with Ekin's Strain Scaling Law [$F_{\mathrm{PM}}\left(0,\varepsilon_{\mathrm{I}}\right)$ is the maximum volume pinning force at $T = 0$][1,85]. In the simplified Interpolative Scaling Law, $n' = w^{-1}\left[u + 2 + w\left(n-2\right)\right]$ and has values of ~1.1 (EM-LMI) and ~1.2 (Vac).

3.5.2 Parameterisations of partial $J_C(B,T,\varepsilon)$ datasets

An important practical issue in relation to scaling laws for $J_{\mathrm{C}}\left(B,T,\varepsilon\right)$ relates to the accuracy achieved when extrapolating parameterisations of partial datasets. Given the considerable resources involved in obtaining comprehensive $J_{\mathrm{C}}\left(B,T,\varepsilon\right)$ data, it is important to understand the minimum datasets and the types of scaling law that are required for sufficiently accurate predictions to be made. We will investigate this issue by using the simplified Interpolative Scaling Law to fit subsets of the complete $J_{\mathrm{C}}\left(B,T,\varepsilon\right)$ datasets, and then comparing the extrapolations with the measured data in regions of parameter space not included in the fit. Three types of partial dataset will be considered: (a) $J_{\mathrm{C}}\left(B,4.2\ \mathrm{K},\varepsilon\right)$ and $J_{\mathrm{C}}\left(B,T,\varepsilon = \mathrm{constant}\right)$ data (i.e. variable-strain

Table 3.4. Approximate universal values for parameters in the simplified Interpolative Scaling Law used for fitting partial $J_{\mathrm{C}}\left(B,T,\varepsilon\right)$ datasets (the letters in brackets show the partial datasets for which the universal values are required: see Table 3.5).

p	q	n	ν	w	$T^{*}_{\mathrm{C}}\left(0\right)$ (K)
$0.5^{(abc)}$	$2^{(abc)}$	$2.5^{(abc)}$	$1.5^{(abc)}$	$2.2^{(abc)}$	$17.5^{(b)}$
u	c_2	c_3	c_4	c_5	
$0^{(c)}$	$-0.752^{(c)}$	$-0.419^{(c)}$	$0.0611^{(c)}$	$0.0619^{(c)}$	

Table 3.5. RMS errors for extrapolations made from partial datasets using the simplified Interpolative Scaling Law. The extrapolations and fits are limited to $4.2\ \mathrm{K} \le T \le 8\ \mathrm{K}$ and $\left|\varepsilon_{\mathrm{I}}\right| \le 1.1\%$. Also shown are the mean values of I_{C} in the extrapolation regions.

Partial dataset fitted		RMS error for extrapolation (mean I_C) (A)		
		EM-LMI wire	Vac wire	OST wire
(a)	$J_{\mathrm{C}}\left(B,T,\varepsilon_{\mathrm{A}} = 0\right)$ and $J_{\mathrm{C}}\left(B,4.2\ \mathrm{K},\varepsilon_{\mathrm{A}}\right)$	2.6 (38.0)	3.2 (43.0)	3.0 (27.5)
(b)	$J_{\mathrm{C}}\left(B,4.2\ \mathrm{K},\varepsilon_{\mathrm{A}}\right)$	3.7 (38.5)	3.7 (43.0)	7.2 (27.5)
(c)	$J_{\mathrm{C}}\left(B,T,\varepsilon_{\mathrm{A}} = 0\right)$	2.6 (47.5)	5.7 (83.0)	7.0 (50.5)

measurements at 4.2 K combined with variable-temperature measurements at zero applied strain); (b) only $J_C(B, 4.2\,\mathrm{K}, \varepsilon)$ data; (c) only $J_C(B, T, \varepsilon = \text{constant})$ data.

In all three cases, it is necessary to use an appropriate fixed value for the exponent *w*. Based on our comprehensive data for a number of technological wires (EM-LMI, Vac, OST), and consistent with microscopic theory, we propose that $w = 2.2$ is the best "universal" value to take for Nb_3Sn wires characterised by high values of $B^*_{C2}(0,0)$. Variations in *w* of approximately ±20% are observed (and are expected due to variations in the dirtiness of the Nb_3Sn), but it will be shown that this universal value is adequate for the extrapolations carried out below. Although the values of some or all of the exponents *p*, *q*, *n*, and ν can in principle be determined from each of the partial datasets, we have found that more accurate predictions are generally obtained if these exponents are fixed at the universal values shown in Table 3.4. These universal values include the Kramer values of $p = 1/2$ and $q = 2$[64,101], a value of $\nu = 3/2$ that approximately describes (to within ~2%) the Maki-de Gennes relation for $B_{C2}(T)$[92,103,104], and a half-integral value of $n = 5/2$ observed for a number of Nb_3Sn wires[79,91]. It can be seen by comparing Tables 3.3 and 3.4 that there are some differences between the optimum and universal values for these exponents, particularly for the Vac wire. Nevertheless we have found that the universal values are generally closer to the optimum global values required for accurate extrapolations than the values obtained from partial datasets.

In case (a), constraining 5 parameters (*p*, *q*, *n*, ν, *w*) to the universal values described above results in optimum extrapolations, while case (b) also requires a fixed value of $T^*_C(\varepsilon_I = 0)$, for which we propose 17.5 K as the best universal value[8,91]. In case (c) where no variable-strain data are available, universal relations for the strain-dependent parameters are necessary. Figure 3.8 shows evidence of a universal relation for the normalised values of $B^*_{C2}(0, \varepsilon_I)$ in Nb_3Sn wires characterised by high values of upper critical field. This relation can be described by a fifth-order polynomial with values for the coefficients as shown in Table 3.4. Given the accuracy of the fits shown in Table 3.2, we suggest setting $u = 0$, which (together with $w = 2.2$) then gives approximate universal relations for the normalised values of $A(\varepsilon_I) = \text{const}$ and $T^*_C(\varepsilon_I)$. In case (c), an estimate of the equivalent intrinsic strain (i.e. the parameter ε_M) is also required, which can in principle be calculated[127,128] but represents a potentially large additional source of error.

With the appropriate parameters fixed (see Table 3.4), the remaining free parameters can be obtained by fitting the partial datasets. Table 3.5 shows the accuracy of the resulting extrapolations for three different Nb_3Sn wires, where the extrapolations (and the fits) are constrained to the region of parameter space defined by $4.2\,\mathrm{K} \le T \le 8\,\mathrm{K}$ and $|\varepsilon_I| \le 1.1\%$. It can be seen that for case (a) the RMS differences between the calculated and measured values in the extrapolation region are typically ~8% of the mean critical current. The errors are somewhat larger for case (b), particularly for the OST wire where the RMS error is ~25%. Note also that in case (c) it has been assumed that ε_M has been accurately calculated to be the optimum value, although it is found that errors of ±10% in ε_M cause the RMS errors for the extrapolations to increase by ~50%. If the extrapolations are extended to the whole range of parameter space (i.e. $4.2\,\mathrm{K} \le T \le 12\,\mathrm{K}$ and $|\varepsilon_I| \le 1.6\%$) the errors increase further, typically by a factor of ~2.

In conclusion, we propose the simplified Interpolative Scaling Law for parameterising $J_C(B,T,\varepsilon)$ data. For complete datasets, it allows interpolations to be made with an accuracy of ~4% and, with fewer and more easily-determinable free parameters (in relation to the ISL), it facilitates interlaboratory and intersample comparisons. For partial datasets, the simplified Interpolative Scaling Law with appropriate fixed parameters allows extrapolations to be made that are reasonably accurate and extensive: if variable-temperature and variable-strain datasets are available, accuracies of ~8% can be achieved over limited ranges, whereas if only variable-temperature or only variable-strain data are available, the errors increase.

3.6 Conclusions

Comprehensive $J_C(B,T,\varepsilon)$ data are presented for the EM-LMI and Vac Nb_3Sn superconducting wires used in the two ITER model coils. Various consistency tests demonstrate good interlaboratory agreement and that J_C is a single-valued function of B, T, and ε. For high-upper-critical-field (28–30 T) Nb_3Sn wires, we report an approximately universal relationship between normalised $B^*_{C2}(0)$ and intrinsic strain, and a power-law relationship between $B^*_{C2}(0,\varepsilon_I)$ and $T^*_C(\varepsilon_I)$ with a typical value of ~2.2 for the exponent. Both results differ from those obtained previously for binary, low-upper-critical-field (~24 T) Nb_3Sn wires in which $B^*_{C2}(0)$ and T^*_C are less strain-dependent and the power-law exponent is larger (≥ 3). The standard Summers Scaling Law therefore predicts a weaker strain-dependence for J_C and does not accurately fit the $J_C(B,T,\varepsilon)$ data for either the EM-LMI or Vac wires. Analysis of the relationship between $B^*_{C2}(0,\varepsilon_I)$ and $T^*_C(\varepsilon_I)$ using microscopic theory shows that the calculated value for the power-law exponent decreases with increasing impurity scattering rate in agreement with the experimental data, and that the uniaxial strain effects are predominantly due to changes in the average phonon frequencies rather than the electronic density of states at the Fermi energy. We propose a simplified Interpolative Scaling Law to describe $J_C(B,T,\varepsilon)$ in technological Nb_3Sn wires with high values of upper critical field, motivated by microscopic theory and scaling considerations. The scaling law incorporates a polynomial function for normalised $B^*_{C2}(0,\varepsilon_I)$ and modified power-law relations between the strain-dependent variables. It allows accurate (~4%) parameterisations to be made of complete $J_C(B,T,\varepsilon)$ datasets and, with appropriate universal values for some of the parameters, reasonably accurate and extensive predictions to be made from partial datasets.

Appendix: Parameterising variable-strain critical-current data of strands for coils and magnets (Part of University of Durham Report No. EFDA/03-1103)

The "simplified interpolative scaling law" uses the following set of equations to parameterise the critical current density of technological $A15$ (Nb_3Sn and Nb_3Al) strands as a function of magnetic field, temperature, and axial strain (Ref. A1):

$$J_{\mathrm{C}}\left(B,T,\varepsilon_{\mathrm{I}}\right)=A\left(\varepsilon_{\mathrm{I}}\right)\left[T_{\mathrm{C}}^{*}\left(\varepsilon_{\mathrm{I}}\right)\left(1-t^{2}\right)\right]^{2}\left[B_{\mathrm{C2}}^{*}\left(T,\varepsilon_{\mathrm{I}}\right)\right]^{n-3}b^{p-1}\left(1-b\right)^{q} \tag{A20}$$

$$B_{\mathrm{C2}}^{*}\left(T,\varepsilon_{\mathrm{I}}\right)=B_{\mathrm{C2}}^{*}\left(0,\varepsilon_{\mathrm{I}}\right)\left(1-t^{v}\right) \tag{A21}$$

$$\left(\frac{A\left(\varepsilon_{\mathrm{I}}\right)}{A\left(0\right)}\right)^{1/u}=\left(\frac{B_{\mathrm{C2}}^{*}\left(0,\varepsilon_{\mathrm{I}}\right)}{B_{\mathrm{C2}}^{*}\left(0,0\right)}\right)^{1/w}=\frac{T_{\mathrm{C}}^{*}\left(\varepsilon_{\mathrm{I}}\right)}{T_{\mathrm{C}}^{*}\left(0\right)} \tag{A22}$$

$$\frac{B_{\mathrm{C2}}^{*}\left(0,\varepsilon_{\mathrm{I}}\right)}{B_{\mathrm{C2}}^{*}\left(0,0\right)}=1+c_{2}\varepsilon_{\mathrm{I}}^{2}+c_{3}\varepsilon_{\mathrm{I}}^{3}+c_{4}\varepsilon_{\mathrm{I}}^{4}\,. \tag{A23}$$

where: J_{C}: engineering critical current density (Am^{-2}), defined as the critical current divided by the total cross-sectional-area of the wire.

$\varepsilon_{\mathrm{I}}=\varepsilon_{\mathrm{A}}-\varepsilon_{\mathrm{M}}$. ε_{I}: intrinsic strain. ε_{A}: applied strain. ε_{M}: applied strain at the peak (all in units of percent).

T_{C}^{*}: effective critical temperature (K).

$t=T/T_{\mathrm{C}}^{*}$: reduced temperature.

B_{C2}^{*}: effective upper critical field (T).

$b=B/B_{\mathrm{C2}}^{*}$: reduced magnetic field.

The simplified interpolative scaling law involves 13 parameters, the values of which are presented below for a number of Nb_3Sn strands and a Nb_3Al strand (for J_{C} defined at 10 $\mu\mathrm{Vm}^{-1}$).

For parameterising partial datasets, universal values are used for some of the parameters, as described in Ref. A1. For example, where only variable-strain limited-variabl;e-field data at 4.2 K are available, the values $p=0.5$, $q=2$, $n=2.5$, $v=1.5$, $w=2.2$, and $T_{\mathrm{C}}^{*}\left(0\right)=17.5$ K are used (see Table 3 below—Furukawa strand).

1 EM-LMI ITER Nb_3Sn (diameter: 0.81 mm)

Data range parameterised: 0.5 T ≤ B ≤ 23 T, 4.2 K ≤ T ≤ 12 K, −0.81% ≤ ε_A ≤ 0.61%.
RMS difference between measured and calculated values: 1.4 A.

p	Q	n	ν	w	u	ε_M (%)
0.4741	1.953	2.338	1.446	1.936	−0.056	0.2786

$A(0)$ ($Am^{-2}T^{3-n}K^{-2}$)	$T_C^*(0)$ (K)	$B_{C2}^*(0,0)$ (T)	c_2	c_3	c_4
2.446×10^7	16.89	28.54	−0.7697	−0.4913	−0.0538

2 Vac ITER Nb_3Sn (diameter: 0.81 mm)

Data range parameterised: 0.5 T ≤ B ≤ 23 T, 4.2 K ≤ T ≤ 12 K, −1.22% ≤ ε_A ≤ 0.73%.
RMS difference between measured and calculated values: 2.5 A.

p	Q	n	ν	w	u	ε_M (%)
0.4625	1.452	2.457	1.225	2.216	0.051	0.3404

$A(0)$ ($Am^{-2}T^{3-n}K^{-2}$)	$T_C^*(0)$ (K)	$B_{C2}^*(0,0)$ (T)	c_2	c_3	c_4
9.460×10^6	17.58	29.59	−0.6602	−0.4656	−0.1075

3 Furukawa ITER Nb_3Sn (diameter: 0.81 mm)

Data range parameterised: 0.5 T ≤ B ≤ 15 T, T = 4.2 K, −1.22% ≤ ε_A ≤ 0.73%.
RMS difference between measured and calculated values: 2.7 A.

p	q	n	ν	w	u	ε_M (%)
0.5†	2†	2.5†	1.5†	2.2†	0†	0.3152

$A(0)$ ($Am^{-2}T^{3-n}K^{-2}$)	$T_C^*(0)$ (K)	$B_{C2}^*(0,0)$ (T)	c_2	c_3	c_4
1.112×10^7	17.5†	30.90	−0.6451	−0.4192	−0.0814

†Universal values.

4 Sumitomo ITER Nb_3Al (diameter: 0.81 mm)

a) Data range parameterised: 0.5 T ≤ B ≤ 15 T, 4.2 K ≤ T ≤ 14 K, –1.96% ≤ ε_A ≤ 0.73%. RMS difference between measured and calculated values: 1.1 A.

p	q	n	ν	w	u	ε_M (%)
0.6973	2.671	2.651	1.269	1.933	–0.102	0.1609

$A(0)$ ($Am^{-2}T^{3-n}K^{-2}$)	$T_C^*(0)$ (K)	$B_{C2}^*(0,0)$ (T)	c_2	c_3	c_4
2.564×10^7	15.68	26.81	–0.1050	–0.0074	0.0065

The following represent fits over reduced ranges, as performed in Ref A2:

b) Data range parameterised: 0.5 T ≤ B ≤ 15 T, 4.2 K ≤ T ≤ 10 K, –0.73% ≤ ε_A ≤ 0.73%. RMS difference between measured and calculated values: 0.8 A.

p	q	n	ν	w	u	ε_M (%)
0.7292	2.762	2.632	1.258	2.021	–0.687	0.1479

$A(0)$ ($Am^{-2}T^{3-n}K^{-2}$)	$T_C^*(0)$ (K)	$B_{C2}^*(0,0)$ (T)	c_2	c_3	c_4
2.869×10^7	15.67	27.23	–0.1116	0.0116	0.0264

c) Data range parameterised: 0.5 T ≤ B ≤ 15 T, 4.2 K ≤ T ≤ 10 K, –1.96% ≤ ε_A < –0.73%. RMS difference between measured and calculated values: 0.8 A.

p	q	n	ν	w	u	ε_M (%)
0.4666	2.191	2.940	1.204	1.884	–0.107	0.1609

$A(0)$ ($Am^{-2}T^{3-n}K^{-2}$)	$T_C^*(0)$ (K)	$B_{C2}^*(0,0)$ (T)	c_2	c_3	c_4
7.365×10^6	16.52	26.81	–0.2326	–0.1275	–0.0229

5 OST Nb_3Sn (diameter: 0.5 mm)

Data range parameterised: 0.5 T ≤ B ≤ 15 T, 4.2 K ≤ T ≤ 12 K, −1.22% ≤ ε_A ≤ 0.49%.
RMS difference between measured and calculated values: 1.7 A.

p	q	n	ν	w	u	ε_M (%)
0.4763	2.150	3.069	1.240	2.545	–0.912	0.2421

$A(0)$ ($Am^{-2}T^{3-n}K^{-2}$)	$T_C^*(0)$ (K)	$B_{C2}^*(0,0)$ (T)	c_2	c_3	c_4
6.417×10^6	18.00	29.17	–0.6457	–0.4514	–0.1009

Ref. A1: D. M. J. Taylor and D. P. Hampshire, Phys. Rev. B (In progress September 2004)
Ref. A2: Keys, N. Koizumi, and D. P. Hampshire, Supercond. Sci. Tech. **15**, 991 (2002)

REFERENCES

[1] J. W. Ekin, Cryogenics **20**, 611 (1980).

[2] J. W. Ekin, Adv. Cryo. Eng. **30**, 823 (1984).

[3] N. Mitchell, Fusion Eng. Des. **66-8**, 971 (2003).

[4] R. Zanino and L. Savoldi-Richard, Cryogenics **43**, 91 (2003).

[5] R. Zanino, N. Mitchell, and L. Savoldi-Richard, Cryogenics **43**, 179 (2003).

[6] M. Takayasu, R. A. Childs, R. N. Randall, R. J. Jayakumar, and J. V. Minervini, IEEE Trans. Appl. Supercond. **9**, 644 (1999).

[7] M. Spadoni (private communication).

[8] A. Godeke and H. G. Knoopers, University of Twente Report No. UT-NET 98-5 (1998).

[9] A. Martínez and J. L. Duchateau, Cryogenics **37**, 865 (1997).

[10] W. Specking, J. L. Duchateau, and P. Decool, in *Proceedings of the 15th International Conference on Magnet Technology*, edited by L. Liangzhen, S. Guoliao, and Y. Luguang (Science Press, Beijing, 1998), p. 1210.

[11] D. P. Hampshire, D. M. J. Taylor, P. Foley, and S. A. Keys, University of Durham Report No. DurSC0601 (2001).

[12] D. M. J. Taylor and D. P. Hampshire, Physica C **401**, 40 (2003).

[13] A. Godeke and H. J. G. Krooshoop, University of Twente Report No. UT-NET/EFDA 2000-5 (2000).

[14] B. ten Haken, A. Godeke, and H. H. J. ten Kate, J. Appl. Phys. **85**, 3247 (1999).

[15] D. M. J. Taylor and D. P. Hampshire, (In progress September 2004).

[16] N. Cheggour and D. P. Hampshire, J. Appl. Phys. **86**, 552 (1999).

[17] H. J. N. van Eck, D. C. van der Laan, M. Dhallé, B. tenHaken, and H. H. J. ten Kate, Supercond. Sci. Tech. **16**, 1026 (2003).

[18] D. Uglietti, B. Seeber, V. Abacherli, A. Pollini, D. Eckert, and R. Flukiger, Supercond. Sci. Tech. **16**, 1000 (2003).

[19] C. R. Walters, I. M. Davidson, and G. E. Tuck, Cryogenics **26**, 406 (1986).

[20] T. Luhman, M. Suenaga, and C. J. Klamut, Adv. Cryo. Eng. **24**, 325 (1978).

[21] G. Rupp, IEEE Trans. Appl. Supercond. **13**, 1565 (1977).

[22] B. ten Haken, PhD Thesis, University of Twente, 1994.

[23] D. M. Kroeger, D. S. Easton, A. DasGupta, C. C. Koch, and J. O. Scarbrough, J. Appl. Phys. **51**, 2184 (1980).

[24] J. W. Ekin and S. L. Bray, Adv. Cryo. Eng. **42**, 1407 (1996).

[25] S. T. Wang, R. Wahrer, C. J. Chen, T. S. Tenforde, R. M. Scanlan, J. W. Ekin, and S. Bray, IEEE Trans. Magn. **30**, 2344 (1994).

[26] R. Flukiger, in *Handbook of Superconducting Materials*; *Vol. 1*, edited by D. Cardwell and D. Ginley (IOP Publishing, Bristol, 2003), p. 391.

[27] J. W. Ekin, F. R. Fickett, and A. F. Clark, Adv. Cryo. Eng. **22**, 449 (1975).

[28] S. A. Keys, N. Koizumi, and D. P. Hampshire, Supercond. Sci. Tech. **15**, 991 (2002).

[29] T. Takeuchi, Y. Iijima, K. Inoue, H. Wada, B. ten Haken, H. H. J. ten Kate, K. Fukuda, G. Iwaki, S. Sakai, and H. Moriai, Appl. Phys. Lett. **71**, 122 (1997).

[30] T. Kuroda, H. Wada, Y. Iijima, and K. Inoue, J. Appl. Phys. **65**, 4445 (1989).

[31] W. Goldacker, W. Specking, F. Weiss, G. Rimikis, and R. Flukiger, Cryogenics **29**, 955 (1989).

[32] J. W. Ekin, T. Yamashita, and K. Hamasaki, IEEE Trans. Magn. **21**, 474 (1985).

[33] W. Goldacker and S. I. Schlachter, Physica C **378–381**, 889 (2002).

[34] H. Kitaguchi, A. Matsumoto, H. Hatakeyama, and H. Kumakura, Supercond. Sci. Tech. **16**, 976 (2003).

[35] J. W. Ekin, D. K. Finnemore, Q. Li, J. Tenbrink, and W. Carter, Appl. Phys. Lett. **61**, 858 (1992).

[36] W. Goldacker, J. Kessler, B. Ullmann, E. Mossang, and M. Rikel, IEEE Trans. Appl. Supercond. **5**, 1834 (1995).

[37] H. Kitaguchi, K. Itoh, H. Kumakura, T. Takeuchi, K. Togano, and H. Wada, IEEE Trans. Appl. Supercond. **11**, 3058 (2001).

[38] M. Suenaga, Y. Fukumoto, P. Haldar, T. R. Thurston, and U. Wildgruber, Appl. Phys. Lett. **67**, 3025 (1995).

[39] R. Passerini, M. Dhallé, E. Giannini, G. Witz, B. Seeber, and R. Flukiger, Physica C **371**, 173 (2002).

[40] N. Cheggour, J. W. Ekin, C. C. Clickner, D. T. Verebelyi, C. L. H. Thieme, R. Feenstra, and A. Goyal, Appl. Phys. Lett. **83**, 4223 (2003).

[41] W. Goldacker, in *Handbook of Superconducting Materials*; *Vol. 2*, edited by D. Cardwell and D. S. Ginley (IOP, Bristol, 2003), p. 1527.

[42] N. Cheggour and D. P. Hampshire, Rev. Sci. Instrum. **71**, 4521 (2000).

[43] A. Godeke, M. Dhallé, A. Morelli, L. Stobbelaar, H. van Weeren, H. J. N. van Eck, W. Abbas, A. Nijhuis, A. den Ouden, and B. ten Haken, Rev. Sci. Instrum. (to be published 2004).

[44] L. F. Goodrich and F. R. Fickett, Cryogenics **22**, 225 (1982).

[45] J. W. Ekin, J. Appl. Phys. **49**, 3406 (1978).

[46] M. Polak, W. Zhang, J. Parrell, X. Y. Cai, A. Polyanskii, E. E. Hellstrom, D. C. Larbalestier, and M. Majoros, Supercond. Sci. Tech. **10**, 769 (1997).

[47] International Electrotechnical Commission Report No. 61788-2 (First edition) (1999).

[48] H. Wada, L. F. Goodrich, C. Walters, and K. Tachikawa, Cryogenics **35**, S105 (1995).

[49] D. M. J. Taylor, S. A. Keys, and D. P. Hampshire, Physica C **372**, 1291 (2002).

[50] A. Vostner (private communication).

[51] B. ten Haken, A. Godeke, H. H. J. ten Kate, and W. Specking, IEEE Trans. Magn. **32**, 2739 (1996).

[52] D. M. J. Taylor and D. P. Hampshire, Supercond. Sci. Tech. (submitted September 2004).

[53] F. Mathu and H. C. Meijer, Cryogenics **22**, 428 (1982).

[54] J. Yeager and M. A. Hrusch-Tupta, *Fifth Edition, Low Level Measurements*, 5th ed. (Keithley Instruments, Inc., Cleveland, OH, 2000).

[55] NIST; *Vol. 2004*.

[56] R. C. Rice, J. L. Jackson, J. Bakuckas, and S. Thompson, U.S. Department of Transportation, Federal Aviation Administration Report No. DOT/FAA/AR-MMPDS-01 (2003).

[57] A. F. Clark, in *Materials at Low Temperatures*, edited by R. P. Reed and A. F. Clark (American Society for Metals, Metals Park, OH, 1983), p. 75.

[58] MatWeb; *Vol. 2004*.

[59] N. Mitchell, ITER JCT Report No. 01/06/04 (2004).

[60] A. Nyilas, in *Advances in Cryogenic Engineering: Transactions of the International Cryogenic Materials Conference 2003*; *Vol. 50*, edited by U. B. Balachandran (Springer-Verlag, New York, 2004), p. 151.

[61] A. Nyilas, K. Osamura, and M. Sugano, Supercond. Sci. Tech. **16**, 1036 (2003).

[62] D. M. J. Taylor, S. A. Keys, and D. P. Hampshire, Cryogenics **42**, 109 (2002).

[63] S. A. Keys and D. P. Hampshire, in *Handbook of Superconducting Materials*; *Vol. 2*, edited by D. Cardwell and D. Ginley (IOP Publishing, Bristol, 2003), p. 1297.

[64] E. J. Kramer, J. Appl. Phys. **44**, 1360 (1973).

[65] Anonymous, Vishay Measurements Group Report No. TN-504 (Appendix) (2004).

[66] J. L. Duchateau, M. Spadoni, E. Salpietro, D. Ciazynski, M. Ricci, P. Libeyre, and A. della Corte, Supercond. Sci. Tech. **15**, R17 (2002).

[67] T. Miyazaki, T. Hase, and T. Miyatake, in *Handbook of Superconducting Materials*; *Vol. 2*, edited by D. Cardwell and D. Ginley (IOP Publishing, Bristol, 2003), p. 639.

[68] P. J. Lee and D. C. Larbalestier, IEEE Trans. Appl. Supercond. **11**, 3671 (2001).

[69] H. Ford, *Advanced Mechanics of Materials*, 1st ed. (Longmans Green and Co, London, 1963).

[70] A. Godeke, B. ten Haken, and H. H. J. ten Kate, Physica C **372 - 376**, 1295 (2002).

[71] D. O. Welch, Adv. Cryo. Eng. **26**, 48 (1980).

[72] B. ten Haken, A. Godeke, and H. H. J. ten Kate, IEEE Trans. Magn. **30**, 1867 (1994).

[73] S. Murase, H. Okamoto, T. Wakasa, T. Tsukii, and S. Shimamoto, IEEE Trans. Appl. Supercond. **13**, 3386 (2003).

[74] W. Goldacker and R. Flukiger, IEEE Trans. Magn. **21**, 807 (1985).

[75] W. D. Markiewicz, Cryogenics **44**, 767 (2004).

[76] B. ten Haken, A. Godeke, and H. H. J. ten Kate, IEEE Trans. Appl. Supercond. **5**, 1909 (1995).

[77] W. Turner, (1983).

[78] W. A. Fietz and W. W. Webb, Phys. Rev. **178**, 657 (1969).

[79] D. P. Hampshire, H. Jones, and E. W. J. Mitchell, IEEE Trans. Magn. **21**, 289 (1984).

[80] D. S. Easton and R. E. Schwall, Appl. Phys. Lett. **29**, 319 (1976).

[81] E. Buehler and H. J. Levinstein, J. Appl. Phys. **36**, 3856 (1965).

[82] J. W. Ekin, Appl. Phys. Lett. **29**, 216 (1976).

[83] I. L. McDougall, IEEE Trans. Magn. **11**, 1467 (1975).

[84] G. Rupp, IEEE Trans. Magn. **15**, 189 (1979).

[85] L. T. Summers, M. W. Guinan, J. R. Miller, and P. A. Hahn, IEEE Trans. Magn. **27**, 2041 (1991).

[86] ITER, Design Requirements and Guidelines Level 1 (Annex) (2002).

[87] J. W. Ekin, J. Appl. Phys. **62**, 4829 (1987).

[88] K. Katagiri, T. Kuroda, H. Wada, H. S. Shin, K. Watanabe, K. Noto, Y. Shoji, and H. Seto, IEEE Trans. Appl. Supercond. **5**, 1900 (1995).

[89] B. ten Haken, A. Godeke, and H. H. J. ten Kate, in *Proceedings of EUCAS 1995, the 2nd European Conference on Applied Superconductivity*, edited by D. Dew-Hughes (IOP Publishing, Bristol, 1995), p. 85.

[90] K. C. Lim, J. D. Thompson, and G. W. Webb, Phys. Rev. B **27**, 2781 (1983).

[91] S. A. Keys and D. P. Hampshire, Supercond. Sci. Tech. **16**, 1097 (2003).

[92] E. Helfand and N. R. Werthamer, Phys. Rev. **147**, 288 (1966).

[93] D. O. Welch, IEEE Trans. Magn. **21**, 827 (1985).

[94] P. B. Allen and R. C. Dynes, Phys. Rev. B **12**, 905 (1975).

[95] W. L. McMillan, Phys. Rev. **167**, 331 (1968).

[96] J. P. Carbotte, Rev. Mod. Phys. **62**, 1027 (1990).

[97] T. P. Orlando, E. J. McNiff, S. Foner, and M. R. Beasley, Phys. Rev. B **19**, 4545 (1979).

[98] A. Nijhuis, presented at ITER meeting, Naka, Japan, 2003 (unpublished).

[99] H. Wada, L. F. Goodrich, C. Walters, and K. Tachikawa, Cryogenics **35**, S65 (1995).

[100] E. D. Marquandt, J. P. Lee, and R. Radebaugh, in *Cryocooler 11*, edited by R. G. Ross Jr. (Kluwer Academic/Plenum Publishers, New York, 2001), p. 681.

[101] D. Dew-Hughes, Philos. Mag. **30**, 293 (1974).

[102] J. Bardeen, L. N. Cooper, and J. R. Schrieffer, Phys. Rev. **108**, 1175 (1957).

[103] P. G. De Gennes, Phys. Kondens. Mater. **3**, 79 (1964).

[104] K. Maki, Physics **1**, 21 (1964).

[105] A. Godeke, M. C. Jewell, A. A. Golubov, B. Ten Haken, and D. C. Larbalestier, Supercond. Sci. Tech. **16**, 1019 (2003).

[106] E. L. Wolf, J. Zasadzinski, G. B. Arnold, D. F. Moore, J. M. Rowell, and M. R. Beasley, Phys. Rev. B **22**, 1214 (1980).

[107] J. Kwo and T. H. Geballe, Phys. Rev. B **23**, 3230 (1981).

[108] J. Kwo, T. P. Orlando, and M. R. Beasley, Phys. Rev. B **24**, 2506 (1981).

[109] M. Suenaga, D. O. Welch, R. L. Sabatini, O. F. Kammerer, and S. Okuda, J. Appl. Phys. **59**, 840 (1986).

[110] L. R. Testardi, Rev. Mod. Phys. **47**, 637 (1975).

[111] L. R. Testardi, Phys. Rev. B **5**, 4342 (1972).

[112] L. R. Testardi, in *Physical Acoustics*; *Vol. 10*, edited by W. P. Mason and R. N. Thurston (Academic, New York, 1973), p. 193.

[113] J. R. Patel and B. W. Batterman, Phys. Rev. **148**, 662 (1966).

[114] M. Poirier, F. Laroche, M. Martin, and J. F. Bussiere, Appl. Phys. Lett. **47**, 92 (1985).

[115] M. Weger and I. B. Goldberg, in *Solid State Physics*; *Vol. 28*, edited by H. Ehrenreich, F. Seitz, and D. Turnbull (Academic, New York, 1973), p. 1.

[116] B. M. Klein, L. L. Boyer, D. A. Papaconstantopoulos, and L. F. Mattheiss, Phys. Rev. B **18**, 6411 (1979).

[117] W. Weber and L. F. Mattheiss, Phys. Rev. B **25**, 2270 (1982).

[118] B. Sadigh and V. Ozolins, Phys. Rev. B **57**, 2793 (1998).

[119] L. F. Mattheiss and W. Weber, Phys. Rev. B **25**, 2248 (1982).

[120] L. J. Vieland and A. W. Wicklund, Phys. Lett. **34A**, 43 (1971).

[121] S. Foner and J. McNiff, E.J., Solid State Commun. **39**, 959 (1981).

[122] C. W. Chu and V. Diatschenko, Phys. Rev. Lett. **41**, 572 (1978).

[123] J. J. Hopfield, Phys. Rev. **186**, 443 (1969).

[124] A. Junod, T. Jarlborg, and J. Muller, Phys. Rev. B **27**, 1568 (1983).

[125] B. M. Klein, L. L. Boyer, and D. A. Papaconstantopoulos, Phys. Rev. Lett. **42**, 530 (1979).

[126] D. A. Rudman and M. R. Beasley, Phys. Rev. B **30**, 2590 (1984).

[127] S. Ochiai, K. Osamura, and K. Watanabe, J. Appl. Phys. **74**, 440 (1993).

[128] D. S. Easton, D. M. Kroeger, W. Specking, and C. C. Koch, J. Appl. Phys. **51**, 2748 (1980).